ČESKÉ VYSOKÉ UČENÍ TECHNICKÉ V PRAZE

FAKULTA STROJNÍ

ZÁVĚREČNÁ PRÁCE

2019

RADOMÍR FILIP

ZADÁNÍ DIPLOMOVÉ PRÁCE

ČVUT
České vysoké
učení technické
v Praze

I. OSOBNÍ A STUDIJNÍ ÚDAJE

Příjmení: **Filip** Jméno: **Radomír** Osobní číslo: **408687**

Fakulta/ústav: **Fakulta strojní**

Zadávající katedra/ústav: **Ústav procesní a zpracovatelské techniky**

Studijní program: **Strojní inženýrství**

Studijní obor: **Procesní technika**

II. ÚDAJE K DIPLOMOVÉ PRÁCI

Název diplomové práce:

Modelování pohybu makrořas s využitím CFD

Název diplomové práce anglicky:

Modeling macroalgae motion using CFD

Pokyny pro vypracování:

- Popište možné přístupy k modelování pohybu tuhých nebo elastických látek v kapalině.
- Vytvořte model v systému StarCCM+ pro zvolenou geometrii.
- Proveďte numerické simulace a vyhodnoťte výsledky.
- Popište podrobně použitou metodiku a navrhněte případná zlepšení zvoleného přístupu.

Seznam doporučené literatury:

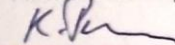Jméno a pracoviště vedoucí(ho) diplomové práce:

Ing. Karel Petera, Ph.D., ústav procesní a zpracovatelské techniky FS

Jméno a pracoviště druhé(ho) vedoucí(ho) nebo konzultanta(ky) diplomové práce:

Datum zadání diplomové práce: **23.10.2018** Termín odevzdání diplomové práce: **11.01.2019**

Platnost zadání diplomové práce: _____

_____ _____ _____
Ing. Karel Petera, Ph.D. prof. Ing. Tomáš Jirout, Ph.D. prof. Ing. Michael Valášek, DrSc.
podpis vedoucí(ho) práce podpis vedoucí(ho) ústavu/katedry podpis děkana(ky)
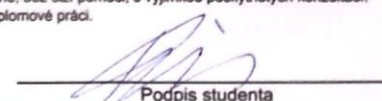
III. PŘEVZETÍ ZADÁNÍ

Diplomant bere na vědomí, že je povinen vypracovat diplomovou práci samostatně, bez cizí pomoci, s výjimkou poskytnutých konzultací.
Seznam použité literatury, jiných pramenů a jmen konzultantů je třeba uvést v diplomové práci.

_____30.10.2018_____ _____
Datum převzetí zadání Podpis studenta

Declaration

I declare that I have elaborated the master thesis independently under supervision of master thesis supervisor and I have listed all documentation and literature.

In Prague, 11.1. 2019   Radomír Filip

Signature

Thanks

Special thanks to my thesis supervisor Ing. Karel Petera, Ph.D. for help, valuable advices and comments during the elaboration of the master thesis.

Annotations list

Author's name: Radomír

Author's surname: Filip

Thesis title Czech: Modelování pohybu makrořas s využitím CFD

Thesis title English: Modelling macroalgae motion using CFD

Thesis scope Number of pages: 65
Number of figures: 42
Number of tables: 5
Number of attachments: 2

Academic year: 2018/2019

Language: English

Department: Department of Process Engineering

Study program: Process Engineering

Thesis supervisor: Ing. Karel Petera, Ph.D.

Opponent:

Consultant:

Submitter: Department of Process Engineering

Annotation in Czech: Diplomová práce se zabývá možnostmi využití CFD nástrojů pro simulace pohybu řas v recirkulačních akvatických systémech. Cílem práce je vytvořit numerický model aerovaného tanku s makrořasami pomocí softwaru Star-CCM+, a následně určit korelaci mezi provozními parametry tanku a doby periodického pohybu řas. Takováto korelace by potom měla praktické využití při návrhu procesu kultivace makrořas.

Annotation in English: This thesis deals with potential use of CFD tools for the movement simulation of macroalgae in the recirculation aquatic systems. The main task of this thesis is to create a numerical model of aerated tank with macroalgae using Star-CCM+ software. Furthermore to determine the mathematical correlation between the operation

parameters of the aerated tank and the recirculation period of the macroalgae motion. Such a correlation would have a practical use in design of macroalgae cultivation processes.

Keywords: CFD, Star-CCM+, macroalgae, aerated tank, recirculation aquatic systems

Thesis purpose: Purpose of this thesis is to contribute to the research and development of Integrated Multi Trophic Aquaculture (IMTA) production systems.

Content

List of symbols

T_c	Ratio between light and dark period (recirculation cycle period)	s^{-1}
f_c	Frequency of the cycle	s^{-1}
ρ	Fluid density	kg/m^3
u, v, w	Velocity	m/s
t	time	s
p	Static pressure	Pa
$\bar{\bar{\tau}}$	Viscous stress tensor	Pa
τ	Shear stress	Pa
g	Gravitational acceleration constant	m
F	Representation of outer forces	-
Re	Reynolds number	-
$\bar{u}, \bar{v}, \bar{w}$	Mean velocity	m/s
u', v', w'	Fluctuating velocity	m/s
L	Characteristic dimension	m
v	Kinematic viscosity	m^2/s
μ	Dynamic viscosity	$Pa.s$
μ_t	Turbulent viscosity	m^2/s
μ_P	Poisson's ratio	
x	Dimension co ordinance	m
y	Dimension co ordinance	m
k	Kinetic turbulence energy	J
ε	Dissipation rate	m^2/s^3
ω	Dissipation rate	m^2/s^3
C_μ	k- ε model's constant	-
α^*	Damping turbulent viscosity coefficient	-
u_τ	Friction velocity	$\sqrt{m^3/s}$
κ	Kármán's constant	-
C	constant	-
u^+	Dimensionless velocity	-

y^+	Dimensionless distance	-
m	mass	kg
τ_1, τ_2, τ_3	Particles time step	s
R	radius	m
$v_{Rayleigh}$	Rayleigh wave velocity	m/s
G	Shear modulus	GPa
V	Volume	m^3
$\dot{V}$	Volume flow rate	m^3/s
λ	Bond radius multiplier	-
d_p	Particle's diameter	m
D_c	Cylindrical tank diameter	m

Abbreviations

IMTA	Integrated Multi Trophic Aquaculture
RAS	Recirculation Aquaculture systems
CFD	Computational Fluid Dynamics
DNS	Direct numerical simulation
LES	Large eddy simulation
RANS	Reynolds Average Navier Stokes

Another symbols

∂	Partial derivation
d	derivation
∇	Nabla operator

1 Introduction

This work aims to contribute to the research and development of Integrated Multi Trophic Aquaculture (IMTA) production systems. Such systems represent an emerging research topic due to their biotechnological potential, in animal and human nutrition, with an impact on human health and wellbeing. The possible use of macroalgal biomass as a source of protein in the formulation of feed for fish in aquaculture (recirculation aquaculture systems - RAS) could reduce the pressure both on open sea fishing and on the use of terrestrial and inland water resources.

1.1 Recirculation aquaculture systems – RAS

Recirculation aquaculture is essentially a technology for farming fish or other aquatic organisms by reusing the water in the production. The technology is based on the use of mechanical and biological filters, and the method can in principle be used for any species grown in aquaculture such as fish, shrimps, clams, etc. [9]

Such recirculation aquaculture system can be simplified as a closed loop containing fish tank and tank with algae or other water plants (Figure 1). In this loop fish are fed, produce excrements and CO_2, which is further used as feed for algae. Then due to photosynthesis water is purified and filled with oxygen and other bi-products could be separated used as a fertilizer. The biggest advantage of RAS compared to traditional flow-through systems is low water consumption, as in some regions water has become a limited source. Such comparison of those systems is shown in Table 1.
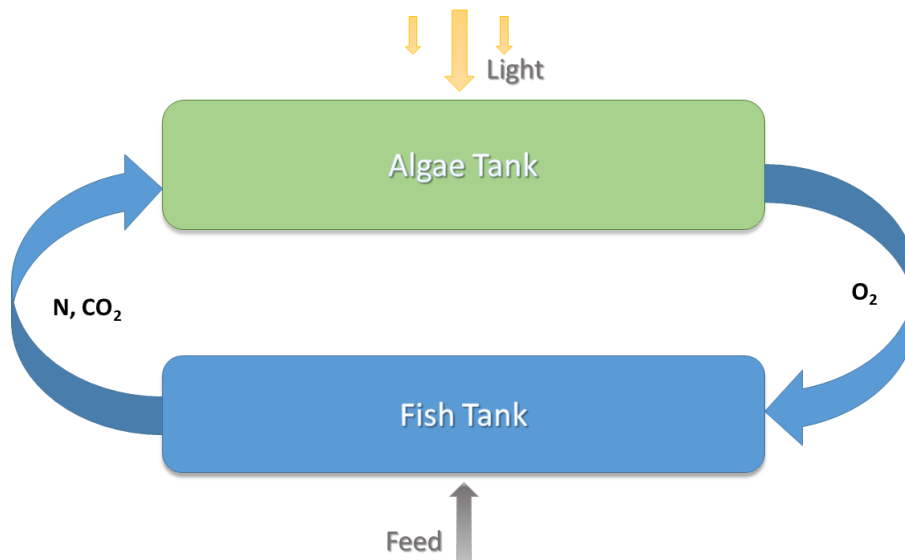
Figure 1: Simplified recirculation aquaculture system.

Type of system	Consumption of new water per kg fish produced per year	Consumption of new water per m³/h	Consumption of new water per day of total system water volume	Degree of recirculation at system volume recycled one time per hour
Flow-through	30 m³	1712 m³/h	1028 %	0 %
RAS low level	3 m³	171 m³/h	103 %	95,9 %
RAS intensive	1 m³	57 m³/h	34 %	98,6 %
RAS super intensive	0,3 m³	17 m³/h	6 %	99,6 %

Table 1: Comparison of degree of recirculation at different intensities compared also to other ways of measuring the rate of recirculation. The calculations are based on a theoretical example of a 500 t/year of produced fish in the system with a total water volume of 4000m³, where 3000m³ is fish tank volume. [9]

1.2 Biological principles in algae production

The central issue involved in mass cultivation of algae concerns effective use of strong light for photosynthetic productivity of cell mass and secondary metabolites. The most important information concerning such a productivity is the measurement of the coupling between photosynthesis and irradiance in form of the steady-state light response curve, which represents the kinetic response of an algal cell to light intensity (Figure 2) [4], [1].

The main features of this curve are as follows: At some very low light intensity, the resulting low growth-rate is balanced by decay and the net growth is zero (compensation point I_c). As light becomes more intense, growth is accelerated, the initial slope of the curve representing maximal efficiency of growth in response to light. With further increase in light intensity, the light saturation function is reached (I_S), at which point the growth rate is the maximal. Further increase in light intensity above this point would not result in further increase in growth rate, but may become injurious, manifested by decreased growth rate due to photo damage [1].
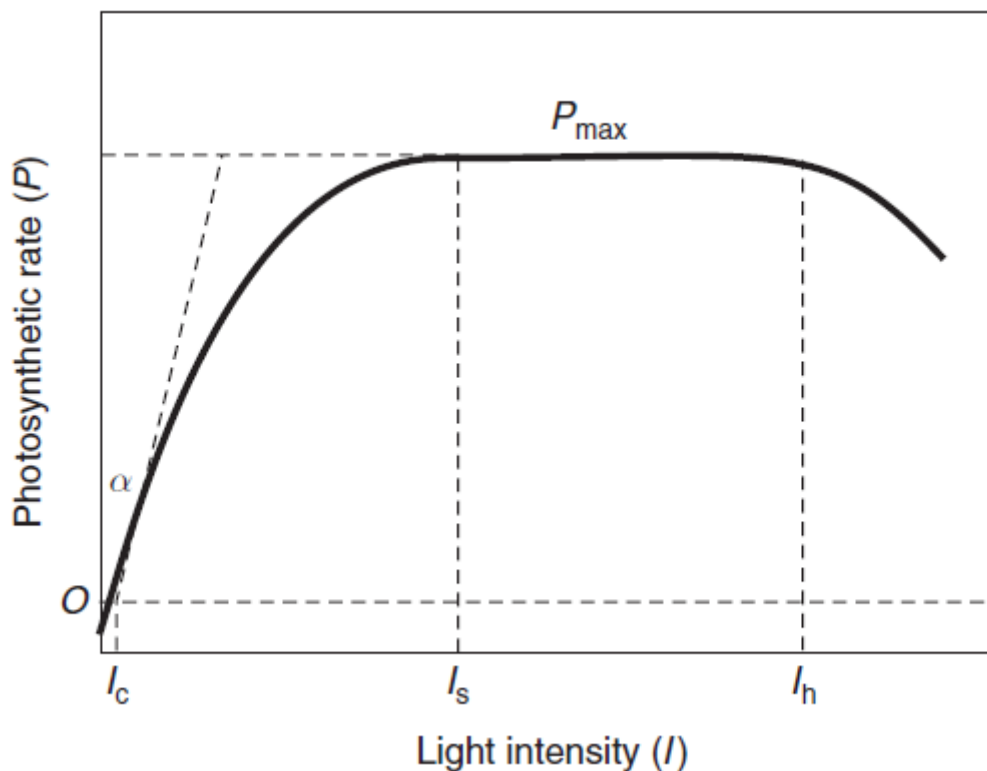

Figure 2: Light response curve of photosynthesis (P-I curve). I_c – light compensation point, I_S – light saturation intensity, I_h – light intensity value at which photo inhibition occurs. [1]

If all growth conditions are optimal (i.e. temperature, amount of nourishments), the intensity of light source is the main factor which controls growth.

In the systems for mass algae cultivation another term needs to be put into the account, which is mutual shading [11]. This phenomena causes internal shadings (Figure 3), which results that cells receiving light intermittently rather than continuously. The higher the cell density, the shorter the depth light penetrates the culture. When mutual shading prevails, cells are rather exposed to cycles of light and darkness (L/D cycle, Figure 4), which may take from milliseconds to a few seconds to complete. Two basic parameters are related to the L/D cycle (having the average irradiance fixed):

- Ratio between the light and the dark period in the cycle.
- Frequency of the cycle $f_c = 1/T_c$.

This results, the higher the frequency of L/D cycle, the more efficient the light may be used for photosynthesis [1].
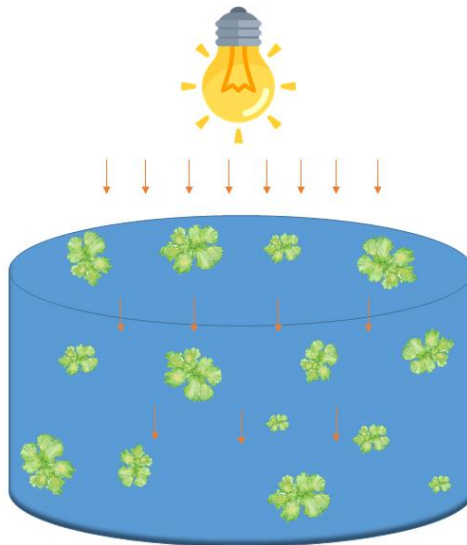
Figure 3: Schematics of mutual shading. The level of irradiance is decreasing with the depth as the photons are absorbed by cells locating in the higher layers of the tank.
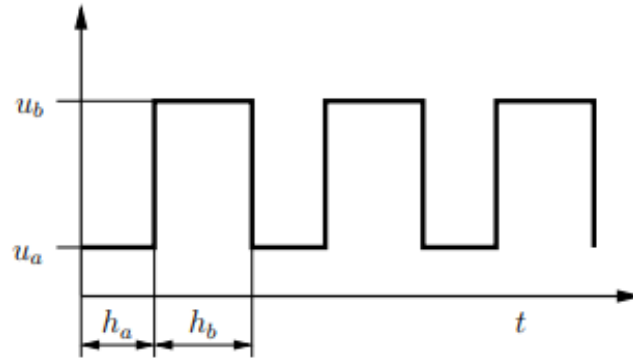
Figure 4: Schematic representation of periodic intermittent input signal u(t): u_a stands for irradiance during period h_a, u_b is irradiance level during period h_b. Total cycle period $T_C = h_a + h_b$. [4]

1.3   Basics of Computational Fluid Dynamics

1.3.1   What is CFD?

CFD is a computer-based tool for analysis of systems involving fluid flow, heat transfer and associated phenomena such as chemical reactions. The technique is very powerful and it is used in vast of industrial and non-industrial applications. Some examples are:

- Aerodynamics of aircraft and vehicles: lift and drag
- Turbomachinery: flows around the turbine vanes
- Chemical process engineering: mixing and separation, polymer molding
- Hydrology and oceanography: flows in rivers and oceans

Thanks to the transistors development in past few decades, the computational power exponentially increased (Moore's law). The high-performance computing hardware has become more available and a combination of user-friendly interface, CFD software have led to an increase of interest in wider industrial community. Although its initial purchasing expenses are high (e.g. commercial software license and suitable hardware), the total expenses are not as great as experimental-based approaches to fluid system design. Moreover, there are several unique advantages of CFD over performing experiments [13]:

- Substantial reduction of lead times and costs of new designs

- Ability to study systems where controlled experiments are difficult or impossible to perform
- Practically unlimited level of detail of results

1.3.2 Governing equations

The fundamental laws that govern the mechanics of fluids and solids are the conservation of mass and momentum.

1.3.2.1 Conservation of Mass

The balance of mass flow through a control volume for compressible fluid is expressed by the continuity equation:

$$\frac{\partial \rho}{\partial t} + \nabla \cdot (\rho \boldsymbol{v}) = 0 \tag{1.1}$$

The first term on left side is the rate of change in time of the density. The second term describes the net flow of mass out of the element across its boundaries and is called the convective term. For incompressible fluid (i.e. a liquid) the density ρ is constant and equation (1) becomes:

$$\nabla \cdot \boldsymbol{v} = 0 \tag{1.2}$$

1.3.2.2 Conservation of momentum

The time rate of change of momentum is equal to the resultant force acting on the continuum and is given by Cauchy momentum equation:

$$\rho \left(\frac{\partial \boldsymbol{v}}{\partial t} + \boldsymbol{v} \cdot \nabla \boldsymbol{v} \right) = -\nabla p + \nabla \cdot \bar{\bar{\tau}} + \rho \boldsymbol{g} + \boldsymbol{F} \tag{1.3}$$

Where p is static pressure, $\bar{\bar{\tau}}$ is viscous stress tensor, $\rho\boldsymbol{g}$ represents gravitational forces and $\boldsymbol{F}$ represents outer forces. These equations along with the conservation of energy equation form a set of coupled, non-linear partial differential equations. It is not possible to solve these equations analytically for most engineering problems. However, it is possible to obtain

approximate computer-based solution to the governing equations for a variety of engineering problems [12].

1.3.3 Finite Volume method

The Finite Volume Method (FVM) is a numerical technique that transforms the partial differential equations representing conservation laws over differential volumes into discrete algebraic equations over finite volumes (or elements or cells). In a similar fashion to the finite difference or finite element method [16], the first step in the solution process is the discretization of the geometric domain, which, in the FVM, is discretized into non-overlapping elements or finite volumes. The partial differential equations are then discretized/transformed into algebraic equations by integrating them over each discrete element. The system of algebraic equations is then solved to compute the values of the dependent variable for each of the elements. These characteristics have made the Finite Volume Method quite suitable for the numerical simulation of a variety of applications involving fluid flow, heat and mass transfer. From a limited potential at inception confined to solving simple physics and geometry over structured grids, the FVM is now capable of dealing with all kinds of complex physics and applications. [14]

1.4 Turbulent flow

1.4.1 What is Turbulence?

The main characteristics of turbulent flow is Reynolds number (1.4). It is a dimensionless number giving a measure of the relative importance of inertia forces and viscous forces.

$$Re = \frac{\bar{u} \cdot L \cdot \rho}{\mu} \tag{1.4}$$

$\bar{u}$ stands for mean velocity, L is characteristic length, ρ is density and μ is dynamic viscosity. In Reynolds experiments (Figure 5) on fluid systems it is observed, that at values below the so-called critical Reynolds number Re_{crit} the flow is smooth and adjacent layers of fluid slide past each other in orderly fashion. That regime is called laminar flow. At values of the Reynold number above Re_{crit}, the flow character is radically changing. It becomes unsteady and in the final state the flow behavior is random and chaotic. This regime is called turbulent flow. [13]
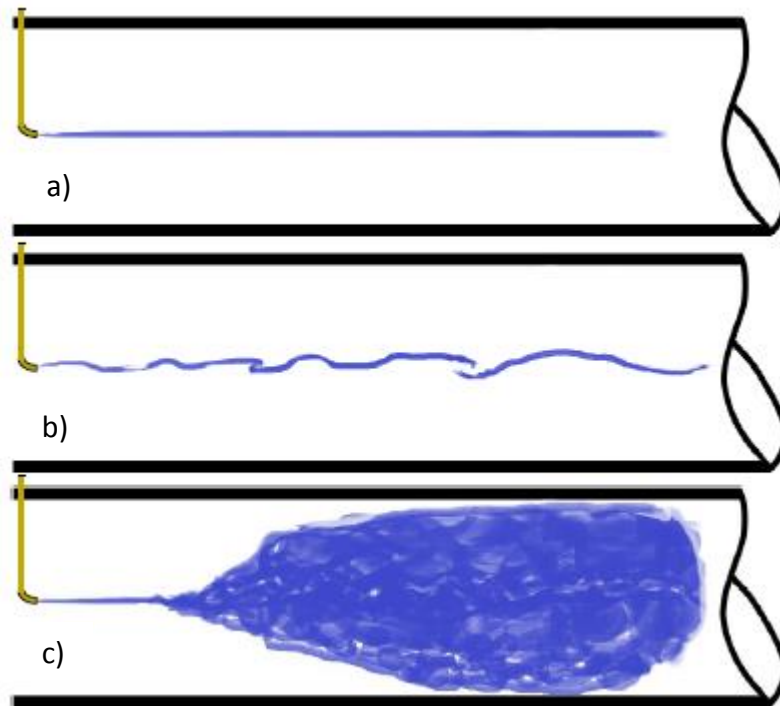
Figure 5: Reynolds experiment: a) Laminar flow (Low Reynolds Number), b) Transitional flow (Increasing Reynolds number), c) Turbulent flow (Higher Reynolds number). [15] Critical Reynolds number for cylindrical pipe is Re_{crit} ~2300.

1.4.2 Turbulence modeling

Turbulence modeling is a crucial issue for the most of CFD simulations. Practically almost all engineering applications work in turbulent flow regime, so that the turbulence model is always required. There is no turbulent model which would be universal for all engineering applications. The choice of the optimal turbulent model depends on flow character, required solution accuracy, available computing hardware and amount of time for simulation. There are three basic approaches to model turbulence and these are Direct Numerical Simulation – DNS, Large Eddy Simulation – LES and Reynolds Averaged Navier-Stokes – RANS. The comparison of accuracies of these methods is shown in Figure 6.
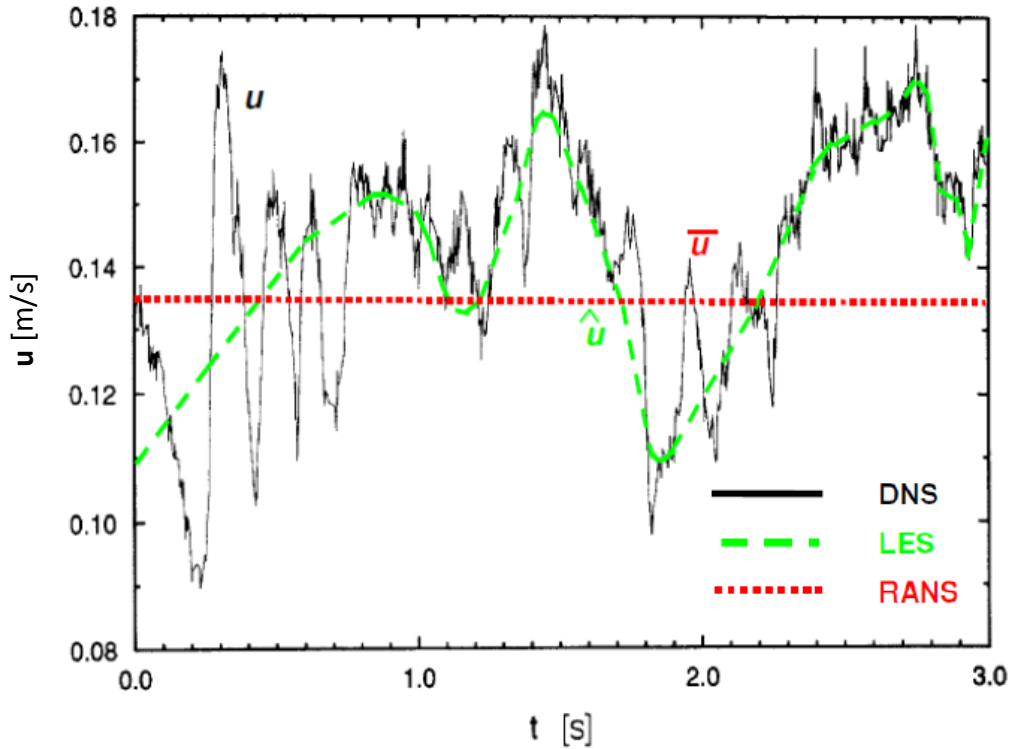
Figure 6: Comparison of turbulence modeling methods.

1.4.3 Direct Numerical Simulation – DNS

The DNS method can theoretically resolve the whole turbulence spectrum of fluctuations by solving Navier-Stokes equation directly with high accuracy. This method requires very fine mesh. The number of elements steadily increase with Reynolds number $N_{DNS} \sim Re^{9/4}$ [17]. The use of DNS method is limited for higher Reynolds number due to big number of elements which need to be resolved. Practically the current technology is not capable to solve DNS with fully developed turbulent flow in any reasonable time. DNS method is nowadays used in special research purposes with fundamentally small systems and low Reynolds numbers.

1.4.4 Large Eddy Simulation – LES

The LES method is based on modeling large eddies, which are spatially and time dependent. Large eddies are solved as DNS. Small scale eddies are isotropic and they are substituted with so-called subgrid-scale models, hence the small eddies can be filtered out of turbulent field. The advantage of LES method is that coarser mesh and bigger time step can be used compared to DNS, that's why highly accurate solutions can be obtained even with the current technologies.

19

1.4.5 Reynolds Averaged Navier-Stokes – RANS

The RANS methods are used for the most of engineering applications. They are offering a quite economical approach for solution of complicated turbulent systems, which are not solvable with LES and DNS methods due to their huge computational requirements. RANS methods are using a so called Reynolds averaging for Navier-Stokes and continuity equations [20], where time averaged variables (e.g. velocity, pressure) and their fluctuations are replaced by specific turbulence model. Such an averaging is shown as an example in typical velocity measurement (Figure 7), where the velocity is fluctuating over the time. If mean velocity from different time periods is taken, then it always leads to the same result. This phenomena was noticed by Osbourne Reynolds, who later suggested that general variable regarding turbulence flow φ could be replaced by its mean value and its fluctuation [17]:

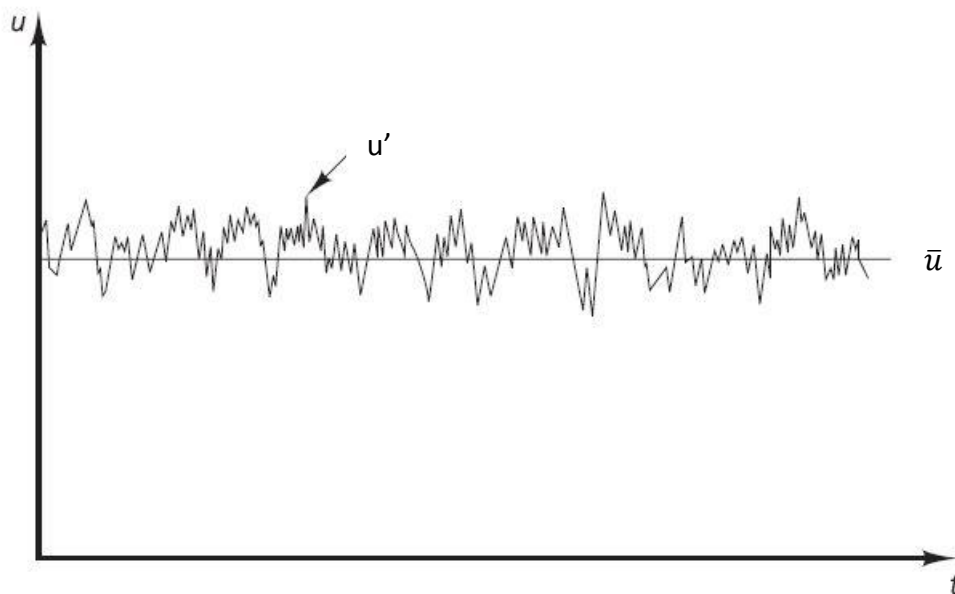*Figure 7: Typical point velocity measurement in turbulent flow. [13]*

$$\varphi = \bar{\varphi} + \varphi'$$
(1.5)

φ' is fluctuation component of general turbulence variable and $\bar{\varphi}$ is time averaged general turbulence variable. At the same time must be valid:

$$\bar{\varphi} = \frac{1}{T} \int_0^t \varphi(t) dt \qquad (1.6)$$

$$\bar{\varphi}' = 0 \qquad (1.7)$$

$$\frac{\partial \bar{\varphi}'}{\partial x} = 0 \qquad (1.8)$$

$$\overline{uv} = \bar{u}\bar{v} + \overline{u'v'} \qquad (1.9)$$

Now when velocity and pressure is applied to the continuity and Navier-Stokes equations according equation (1.5), then their mean form is:

$$\frac{\partial \rho}{\partial t} + \frac{\partial}{\partial x_i}(\rho \bar{u}_\iota) = 0 \qquad (1.10)$$

$$\frac{\partial}{\partial t}(\rho \bar{u}_\iota) + \frac{\partial}{\partial x_j}\left(\rho \bar{u}_\iota \bar{u}_j\right) = -\frac{\partial \bar{p}}{\partial x_i} + \frac{\partial}{\partial x_j}\left[\mu\left(\frac{\partial u_i}{\partial x_j} + \frac{\partial u_j}{\partial x_i} - \frac{2}{3}\delta_{ij}\frac{\partial u_k}{\partial x_k}\right)\right] + \frac{\partial}{\partial x_j}(-\rho \overline{u_\iota' u_j'}) \quad (1.11)$$

Equation (1.11) represents the Averaged Navier-Stokes equation, which is also called Reynolds equation. The last part of equation (1.11) $-\rho\overline{u_i u_j}$ is the stress tensor, which appearance is correlated with velocity fluctuations and it is called Reynolds stresses (τ_{RANS}). In 3D flow this stress tensor contains nine components:

$$\tau_{RANS} = -\rho\overline{u_i' u_j'} = -\rho \cdot \begin{bmatrix} \overline{u'u'} & \overline{u'v'} & \overline{u'w'} \\ \overline{v'u'} & \overline{v'v'} & \overline{v'w'} \\ \overline{w'u'} & \overline{w'v'} & \overline{w'w'} \end{bmatrix} \qquad (1.12)$$

1.4.6 Boussinesq hypothesis

Big majority of RANS turbulence models are based on Boussinesq hypothesis of turbulent viscosity. This hypothesis assumes: As shear stresses in 2D laminar flow could be described with Newton's relation:

$$\tau = \mu \frac{du}{dy} \qquad (1.13)$$

Where τ represents shear stress and μ represents dynamic viscosity. Then this hypothesis assumes that the stress tensor could be replaced by Newton's relation. This means that nine stresses are described by variable which is called turbulent viscosity μ_t.

$$-\rho \overline{u_i' u_j'} = \mu_t \left(\frac{\partial u_i}{\partial x_j} + \frac{\partial u_j}{\partial x_i} \right) - \frac{2}{3} \left(\rho k + \mu_t \frac{\partial u_l}{\partial x_l} \right) \delta_{ij} \qquad (1.14)$$

k is kinetic turbulence energy:

$$k = \frac{1}{2} \overline{u_i' u_j'} = \frac{1}{2} \left(\overline{u'^2} + \overline{v'^2} + \overline{w'^2} \right) \qquad (1.15)$$

Turbulent viscosity is the feature of the turbulent flow (not the liquid) and generally it is function of position and time. [21]

1.4.7 RANS turbulence models

RANS turbulent models are used in most of CFD industry applications. A large number of turbulence models are available, some for very specific applications, other can be applied to a wider range of flows with reasonable degree of confidence. Each CFD software developer such as Ansys or StarCCM+ are able to fit and validate certain model for specific applications. Such a validation of multiple RANS turbulence models is described and shown on Figure 8 [22]. To check which model is useful for which specific application, it is recommended to check the product documentation of each individual software. The basics of k-ε and k-ω models, which can be used for wider range of flows, will be described further.
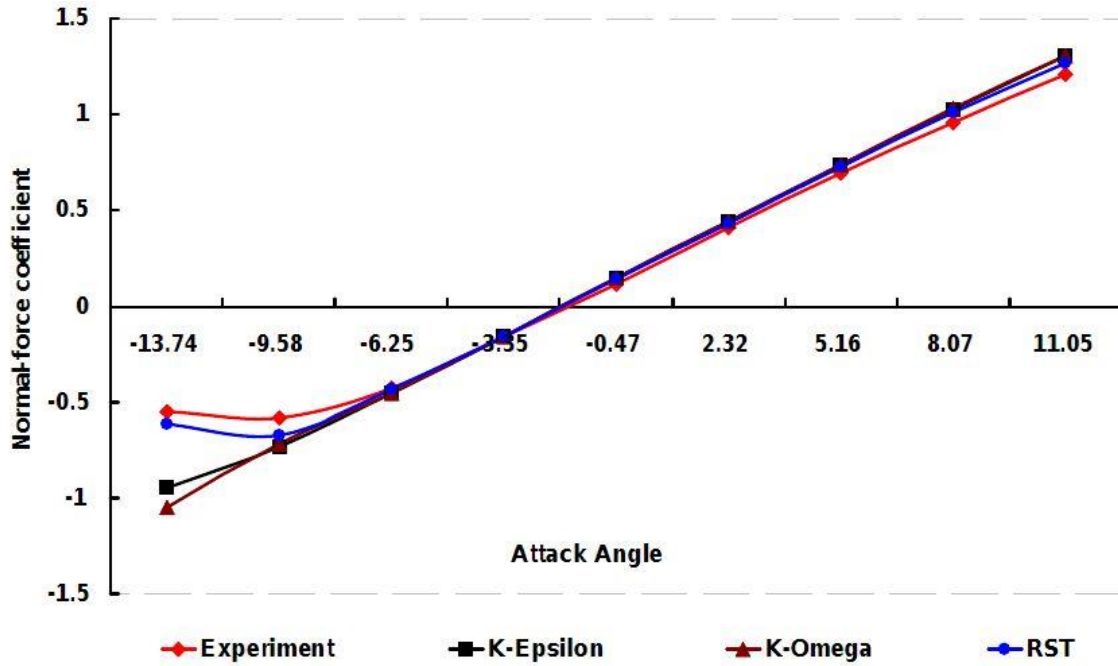
Figure 8: Example of an experimental validation of different RANS turbulence models for use in aero industry. Compared models have good agreements with experimental data. The RST method gave the best results, but K-ω model also gave good results at a much lower computational cost. [22]

1.4.7.1   The *k-ε* model

The *k-ε* models are semi-empiric two-equation turbulence models based on Boussinesq hypothesis. The models solve two additional transport equations [13]. One for turbulent kinetic energy *k* and the other one for the turbulent dissipation rate *ε*. Then the turbulent viscosity μ_t is calculated as:

$$\mu_t = \rho C_\mu \frac{k^2}{\varepsilon} \tag{1.16}$$

C_μ is model's constant. Those constants were obtained from experiments for basic types of turbulent flow. The *k-ε* model contains multiple sub-models such as RNG *k-ε* model and Realizable *k-ε* model, which differ in the model's constants and transport equations to determine *k* and *ε.*

1.4.7.2   The *k-ω* model

The *k-ω* models are semi-empiric two-equation turbulence models based on Boussinesq hypothesis, same as *k-ε* models. The equation model solves transport equations for kinetic energy *k* and specific dissipation rate *ω* – the dissipation rate per unit turbulent kinetic energy ($\omega \approx \varepsilon / k$) in order to determine the turbulent eddy viscosity. Then the turbulent viscosity μ_t for the standard model is calculated as:

$$\mu_t = \alpha^* \frac{\rho k}{\omega} \tag{1.17}$$

Where coefficient α^* is damping turbulent viscosity according correlation for low Reynolds numbers. One reported advantage of the K-Omega model over the K-Epsilon model is its improved performance for boundary layers under adverse pressure gradients. Perhaps the most significant advantage, however, is that it may be applied throughout the boundary layer, including the viscous-dominated region, without further modification. Furthermore, the standard K-Omega model can be used in this mode without requiring the computation of wall distance. The biggest disadvantage of the K-Omega model, in its original form, is that boundary layer computations are sensitive to the values of ω in the free-stream. This translates into extreme sensitivity to inlet boundary conditions for internal flows, a problem that does not exist for the K-Epsilon models.

1.4.8   Turbulence near the wall

Measurements show that, for both internal and external flows, the stream wise velocity in the flow near the wall varies logarithmically with distance from the surface. This behavior is known as the law of the wall [18]. Observation of high Reynolds number turbulent boundary layer shows that, the effects of the fluid's inertia and the pressure gradient are small near the surface. Consequently, the statistics of the flow near the surface in a turbulent boundary layer are established by two primary mechanisms. The first is the rate at which momentum is transferred to the surface, per unit area per unit time, which is equal to the local shear stress τ. The second is molecular diffusion of momentum, which plays an important role very close to the surface. Although τ varies near the surface, the variation with distance from the surface y is slow. Hence the surface shear stress τ_w in place of the local shear stress is used in the dimensional analysis. Then velocity scale u_τ can be derived as:

$$u_\tau = \sqrt{\frac{\tau_w}{\rho}} \qquad\qquad (1.18)$$

Where u_τ is known as the friction velocity and it is a velocity representative of velocities close to a solid boundary. The result of the dimensional analysis is the law of the wall [18]:

$$\frac{\bar{u}}{u_\tau} = \frac{1}{\kappa} \ln \frac{u_\tau y}{\vartheta} + C \qquad\qquad (1.19)$$

Where κ is Kármán's constant and C is a dimensionless integration constant. Correlation of measurements indicate $C \sim 5$ for smooth surfaces and $\kappa \sim 0.41$ for smooth and rough surfaces. [18]

Figure 9 shows a typical velocity profile for a turbulent boundary layer. The graph displays the dimensionless velocity u^+ and distance y^+ defined as:

$$u^+ = \frac{\bar{u}}{u_\tau} \; ; \; y^+ = \frac{u_\tau y}{\vartheta} \qquad\qquad (1.20)$$
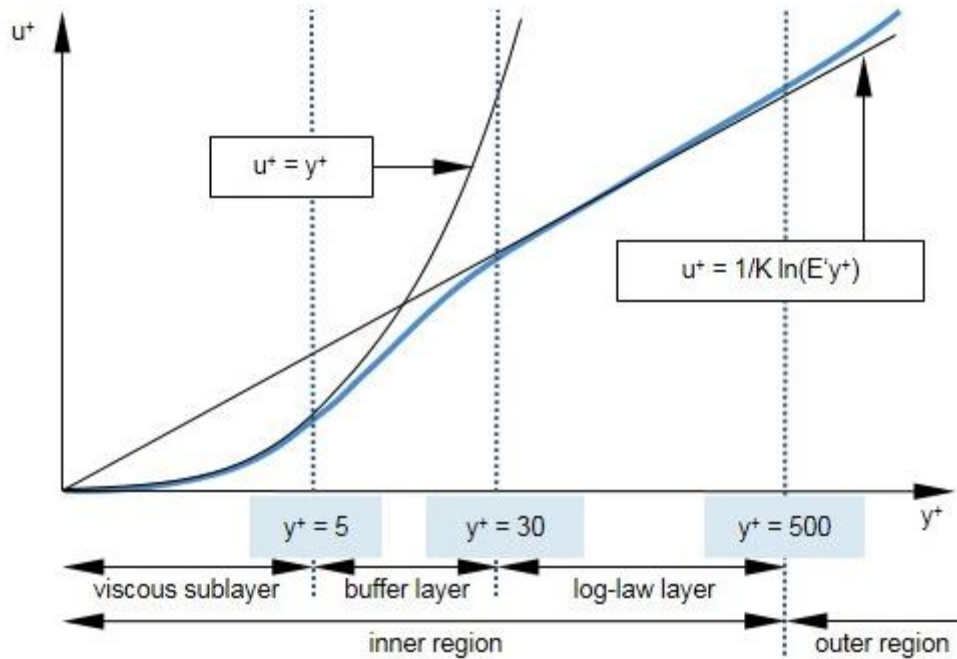
u_τ

Figure 9: Typical velocity profile for a turbulent boundary layer. [23]

The inner region of the boundary layer can be split up into three sublayers. In each of them the flow has different characteristics and can be modeled using different empirical approaches:

- Viscous sublayer: The fluid layer in contact with the wall is dominated by viscous effects and is almost laminar. The mean flow velocity only depends on the fluid, density, viscosity, distance from the wall, and the wall shear stress.
- Log-law layer: The turbulent log-law layer is dominated equally by viscous and turbulent effects.
- Buffer layer: The buffer layer is a transitional layer between the viscous sublayer and the log-law layer.

1.4.8.1 Wall treatment

The software Simcenter Star-CCM+, which is used for computational part of this paper, provides three types of wall treatment:

- The low-y^+ wall treatment resolves the viscous sublayer and needs little or no modeling to predict the flow along the wall boundary. The transport equations are solved all the

26

way to the wall cell. The wall shear stress is computed as in laminar flows. To resolve the viscous sublayer, these models require a sufficiently fine mesh with near-wall cells located at y^+ of around unity. The computational expense that is associated with this approach can be significant, particularly for large Reynolds number flows where the viscous sublayer can be very thin. Therefore, this wall treatment is suitable only for low Reynolds number flows. [23]
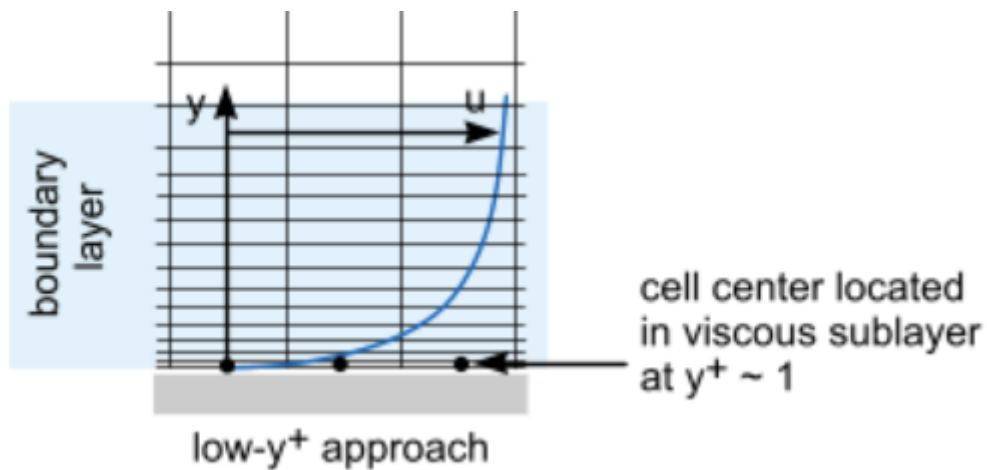

Figure 10: The low-y^+ approach. [23]

- The high-y^+ wall treatment does not resolve the viscous sublayer. Instead wall functions are used to obtain the boundary conditions for the continuum equations. Wall shear stress, turbulent production, and turbulent dissipation are derived from equilibrium turbulent boundary layer theory. This approach assumes that the near-wall cell lies within the log-law layer of the boundary layer at $y^+ > 30$. The main advantage of the high-y^+ wall treatment is therefore the significant savings in the number of near-wall cells. [23]
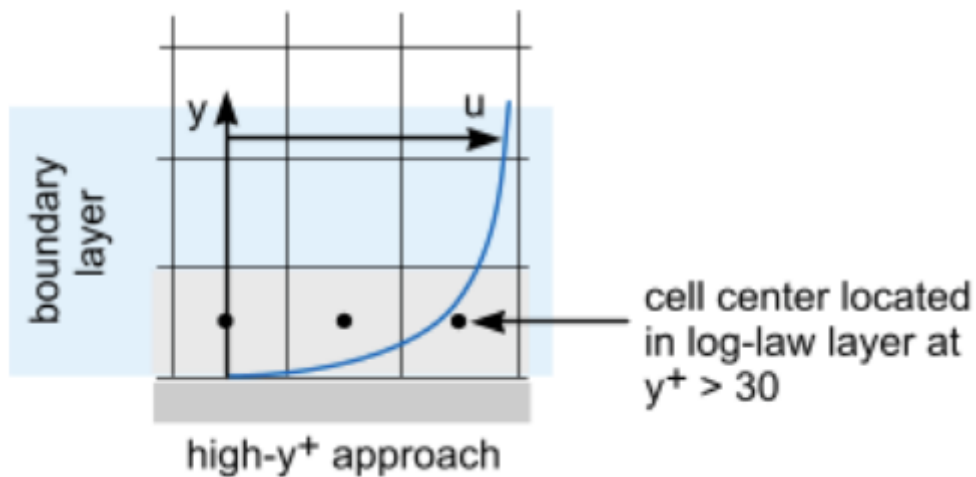

Figure 11: The high-y^+ approach. [23]

- The all-y^+ wall treatment is a hybrid treatment that emulates the low-y^+ wall treatment for fine meshes, and the high-y^+ wall treatment for coarse meshes.

  It is also formulated with the desirable characteristic of producing reasonable answers for meshes of intermediate resolution, that is, when the wall-cell centroid falls within the buffer region of the boundary layer. A blending function is then used to calculate turbulence quantities such as dissipation, production, and stress tensor. [23]
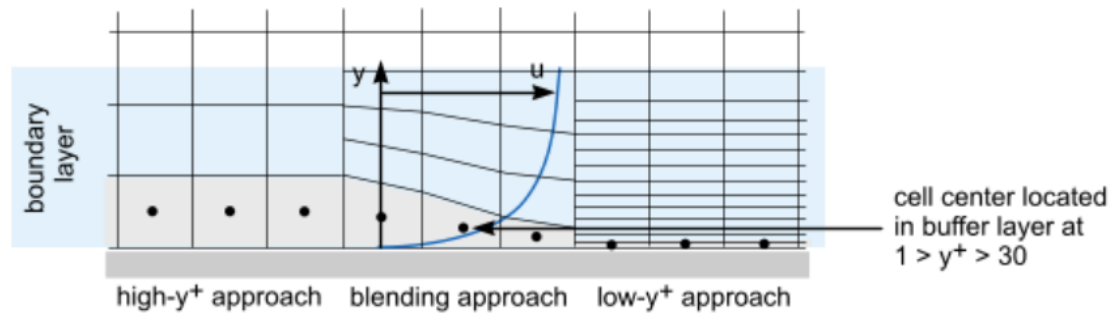

Figure 12: The all-y$^+$ approach. [23]

1.5 Lagrangian multiphase flow

Multiphase flows are found in a wide variety of industrial processes, some examples of which are internal combustion engines, liquid, or solid fueled combustors, spray driers, cyclone dust separators, and chemical reactors. Multiphase in this context refers to one thermodynamic phase, be it a solid, a liquid, or a gas, interacting with another distinct phase. Lagrangian numerical methods can be used in conjunction with Eulerian numerical methods [24] to describe these situations where individual particle dynamics impact the solution on the scale that is resolved in the Eulerian field. Typically, a Lagrangian reference frame is used to describe the evolution of individual particles as they traverse the domain. The equations of change are written following an individual particle. Particles are not resolved on the Eulerian field, they are sub grid and the interaction between the phases is modeled. In general, the continuous phase drives the motion of the dispersed phase. The continuous phase itself is affected by the dispersed phase, as particles occupy volume, and can exchange momentum, heat, and mass with the continuous phase. The strength of the interactions depends on the size, density, and

28

number of dispersed particles. The conservation equation of momentum for a particle is written in the Lagrangian framework. The change in momentum is balanced by surface and body forces that act on the particle. The equation of conservation of (linear) momentum for a material or DEM particle of mass m_p is given by:

$$m_p \frac{dv_p}{dt} = F_s + F_b$$

(1.21)

Where v_p represents the instantaneous particle velocity, F_s is resultant of the forces (e.g. drag force, pressure gradient force) that act on the surface particle and F_b is the resultant of the body forces (e.g. gravity force, contact force). The resultant of the surface forces F_s represents the momentum transfer from the continuous phase to the particle. With one-way coupling, only the continuous phase influences the dispersed phase, but not in the reverse direction. When using the two-way coupling modeling approach, F_s is accumulated over all the parcels and applied in the continuous phase momentum equation. [23]

1.5.1 Discrete Element Method

The discrete element method (DEM) is designed for modeling the granular flow of materials such as sand, food particles, powders, capsules, and slurries. These flows are characterized by a high particle density where the inter-particle interaction is of importance. The DEM model extends the Lagrangian formulation to account for inter-particle interaction in the particle equations of motion. These forces cannot be ignored for highly loaded flows, which are represented by many interacting particles. The DEM particles can assume different shapes and volumes. To represent a DEM particle, the simplest shape is a sphere.

DEM particles models are based on soft-particle formulation in which particles can overlap. The calculated contact force is proportional to the overlap, as well as to the particle material and geometric properties. This contact force enters the Lagrangian momentum equation (1.21) as F_b. The contact force formulation in DEM is typically a variant of the spring-dashpot model (Figure 13). The spring generates repulsive force pushing particles apart and the dashpot represents viscous damping and allows simulation of collision types other than perfectly elastic. The forces at the point of contact are modeled as a pair of spring-dashpot oscillators. A parallel linear spring-dashpot model represents the normal force and a parallel

linear spring-dashpot in series with a slider represents the tangential direction of force with respect to the contact plane normal vector. In both, the spring accounts for the elastic part of the response and the dashpot accounts for energy dissipation during collision. [23]
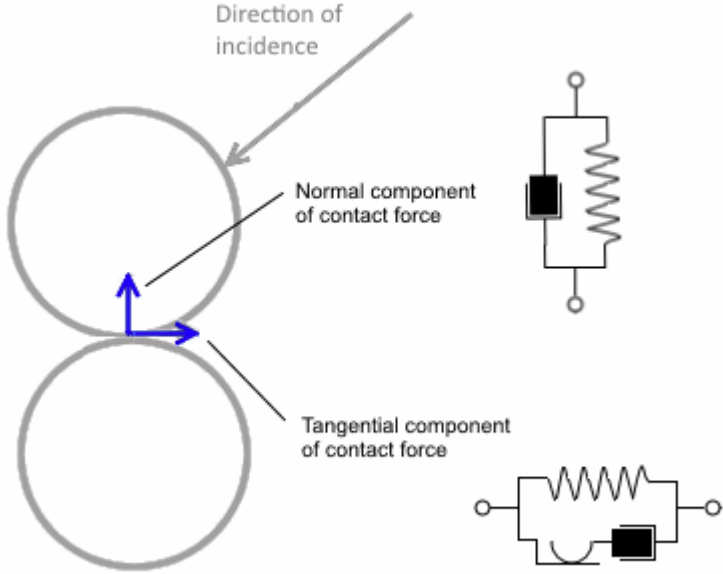

Figure 13: DEM spring-dashpot model. The spring generates repulsive force pushing particles apart and the dashpot represents viscous damping and allows simulation of collision types other than perfectly elastic. [23]

1.5.1.1   Discrete Element Method – Particle Times Scale

To obtain the DEM particle trajectory, equation (1.21) must be integrated over time using a characteristic DEM particle time scale. The particle time scale is the maximum time-step that is allowed for a DEM particle, which is constrained by following assumption: The force acting on a particle is only affected by the particle's immediate neighbors during a single time-step duration [23]. The time-step is therefore limited by the time it takes the Rayleigh wave to propagate across the surface of the sphere to the opposite pole [27]:

$$\tau_1 = \pi \frac{R_{min}}{v_{Rayleigh}}$$

(1.22)

R_{min} is the minimal sphere radius. The Rayleigh wave velocity ($v_{Rayleigh}$) depends on material properties and the exact value is given by equation [28]:

$$v_{Rayleigh} = \sqrt{\left(\frac{G}{\rho}\right) \cdot \left(\frac{0.87 + 1.12 \cdot \mu_P}{1 + \mu_P}\right)} \qquad (1.23)$$

G is shear modulus and μ_P is Poisson's ratio. Besides the wave propagation, more time-step limiting criteria are applied to moving particles. The duration of impact of two perfectly elastic spheres assuming the Hertz contact theory derived by Timoshenko [29] to be:

$$\tau_2 = 2.94 \left(\frac{5\sqrt{2\pi\rho}}{4} \cdot \frac{1 - \mu_P{}^2}{E}\right)^{\frac{2}{5}} \frac{R}{\sqrt[5]{\mu_P}} \qquad (1.24)$$

E is elastic modulus and R is sphere radius. To resolve the collisions, a minimum of 10 time-steps is required. The final restriction on a DEM particle time-step is geometric. It assumes that particles must not move too far within the time-step. This condition prevents missing contacts between DEM particles, as well as particles and walls. Therefore, each particle is constrained such that it takes at least 10 time-steps for the particle to move the full length of the radius.

$$\tau_3 = \frac{R}{v_{Rayleigh}} \qquad (1.25)$$

The final particle time-step is determined as a minimum of τ_1, τ_2, τ_3. In practice τ_1 is typically the limiting factor while τ_2 and τ_3 only constrain particles that are moving fast, or the Young's modulus of the material is set low to accelerate the simulation [23].

2 The objectives and motivation

The motivation of this thesis is to contribute to the research of Integrated Multi Trophic Aquaculture (IMTA) production systems, previously described in chapter (1.1). Unfortunately, this promising field of aquaculture systems, more specifically the macroalgae cultivation and macroalgae photosynthetic growth have lack of mathematical models. The contribution of this work resides in creating such model. The first objective is the analysis of macroalgae motion inside aerated tank using the Star-CCM+ code. Once having determined the complex macroalgae motion, the trajectory of an individual macroalgae can be calculated and subsequently used for the "irradiance history" identification (by a simple concatenation of seaweed trajectory and the irradiance field $I = f (R, t)$ within the device), see [26].

2.1 Expected results

The graphical results from a numerical model should describe the relation between the tank design parameters, operating conditions and flow pattern of the macroalgae motion (time-period of cyclic-rotational motion), as can be seen in Figure 14.
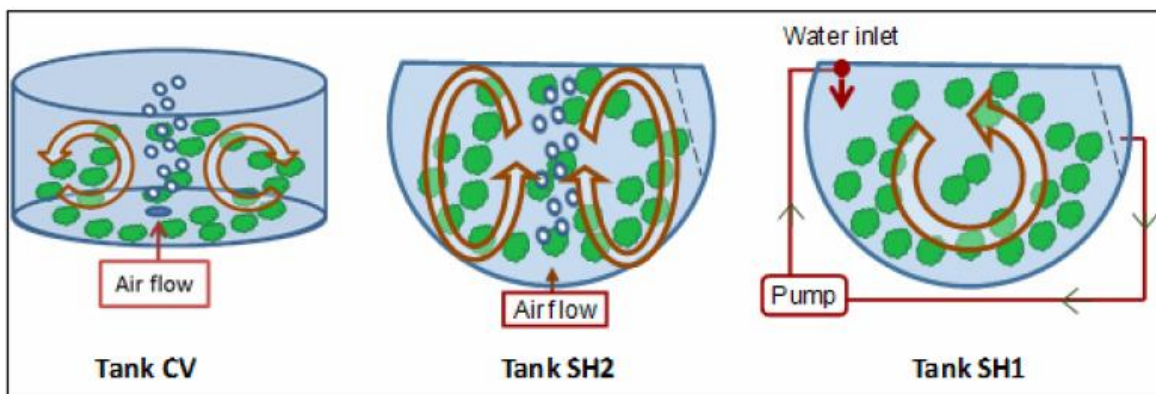

Figure 14: Three laboratory experimental systems: vertical cylindrical (CV) tank, semi-spherical tank bottom aerated (SH2), and semi-spherical tank with water jet system (SH1) [25].

2.1.1 Validation experiment

A validation experiment was performed with cylindrical aerated tank within summer school project [31]. The tank diameter was $d_T =200mm$ with height of the water level $h = d_T$. The air volume rate was approximately $\dot{V}= 50\ l/h.$ Pieces of macroalgae (Ulva ohnoi) were inserted to the tank. Based on the image processing software (developed by Dr. Petr Císař, ICS FFPW USB Nové Hrady), the hydrodynamic pattern of the macroalgae was determined. From the image processing results shown in Figure 15. It is visible that the liquid creates a concentric loop from the top to bottom which in 3D could be visualized as a toroidal shape. The next step is to create numerical simulation matching the same hydrodynamic conditions using Star-CCM+ code.
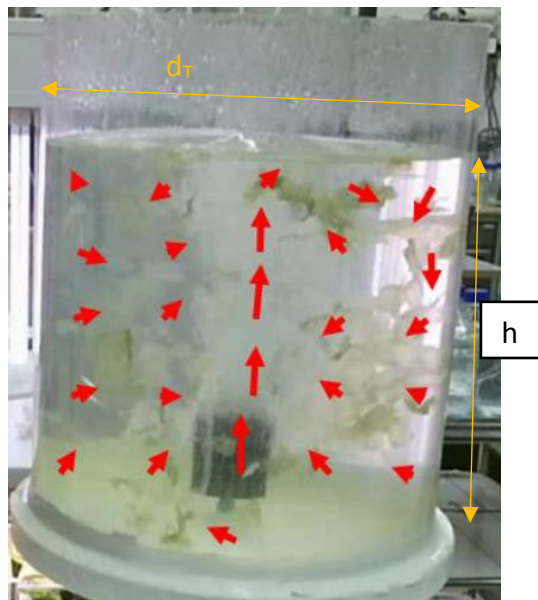
Figure 15: Experimental setup for Ulva ohnoi cultivation - Cylindrical tank with bottom aeration. Result of a project developed within the frame of Schola ludus international summer school for university students organized by University of South Bohemia, Institute of Complex Systems, FFPW.

3 CFD simulation – preprocessing

The method which suits best for the particles tracking like macroalgae, is to use the Lagrangian approach with Discrete Element method – particle clumps model. DEM simulations can become very expensive to run, when many particles are introduced into the domain, and also because of each particle may need a very small time-step to track properly. When considering the thickness of the macroalgae such as Ulva ohnoi, which can be less than 0,1 mm, the number of particles would be "countless", to cover some visible area. Thus the computational time would dramatically rise. However there are some methods that can deliver results in some reasonable time. The flow field will be initialized with steady state two-phase flow, where the gas phase will be modeled with Lagrangian multiphase model. Then the transient physics with DEM model with particle tracking will be applied.

The flow field in the cylindrical tank will be also simulated with usage of inner cylinder assembly, which is expected to improve the flow field for macroalgae growing purposes.

3.1 Speeding up DEM particle clumps simulation

There is one method described in [30], where it is suggested to increase the time step, so that less steps must be solved. This can be approached in two ways:

- Using under-resolving time-steps for the nominal physics.
    - Scaling the calculated time-step by a given factor.
    - Setting a fixed time step for DEM to use regardless of the particle state.
- Using an accurate time-step for slightly different physics.
    - Increasing the particle radius.
    - Decreasing the material stiffness.

Sometimes, reducing the material stiffness by decreasing the Young's Modulus gives the best tradeoff between speed and overall simulation accuracy. Furthermore, the DEM particle type "Particle Clumps" uses a Bonded Particles model which adds a link between linked particles. This can be used to mitigate the effect of using a smaller Young's Modulus [30].

3.1.1 Bonded Particles Formulation

Particles inside the clump are linked by massless beam shown in Figure 16. The beam can transfer forces and moments between the particles. The response to displacements depends on the normal/shear stiffness and on the beam radius $\bar{R} = \lambda R$. Forces are proportional to $\bar{R}^2$ and moments are proportional to $\bar{R}^4$. If a particle's stiffness is changed, a response equivalent to the original stiffness can be obtained by scaling the radius of the beam. This can be done by changing the Bond Radius Multiplier λ in the Particle Clump's self-interaction models. Because forces and moments have a different dependency on the beam radius, either the original force response or the original moment response can be obtained, but not both. [30].

That simply means, if the Young's Modulus is inserted four times bigger than the reference, and at the same time, the Bond Radius Multiplayer 2 times smaller (in case of giving equivalent force response). Then the same original lengthwise stiffness is preserved, but the bending resistance will be now four times smaller, which leads to higher flexibility of the Particle Clumps.
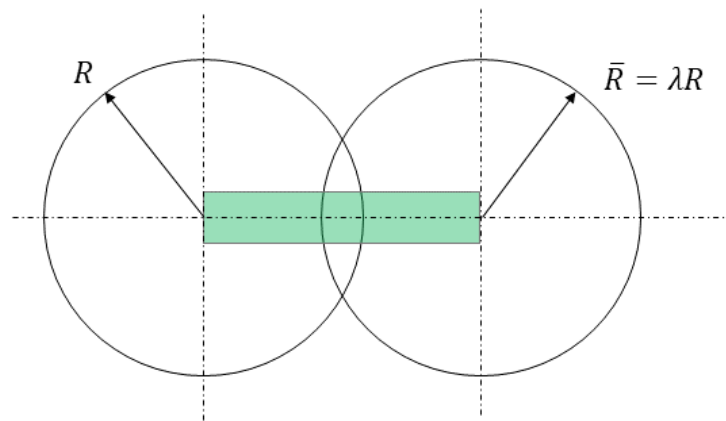
Figure 16: Particles are linked by massless beam (illustrated in green), which can transfer forces and moments between the particles. Default value in Star-CCM+ is $\bar{R} = R(\lambda = 1)$. Where R is the particle radius and λ is the bond radius multiplier. The overlap is necessary.

3.2   Assumptions and simplifications

- The macroalgae geometry is approximated with "chains" of spheres (see Figure 17 and Figure 18). The diameter of spheres is set to 3mm, to maintain low computational time. (<u>overlapping of the spheres is necessary</u>!).

- To prove the DEM concept, firstly the 2D model will be created and tested. Then the 3D model will be created and launched to verify the data from 2D models.

- It is assumed that the particle (solid) movement will not change the flow pattern (liquid) and the interaction between gas and solid can be neglected (Single-phase flow).

- Since the material properties such as Elasticity modulus and Poisson's ratio are unknown for the Ulva ohnoi, the material properties will be set accordingly, to ensure the particle cohesion, flexibility and low computational time.

- Flow field is in steady state and doesn't change in time.

Figure 17: 2D macroalgae geometry. Consists of 25 spheres with 3mm in diameter
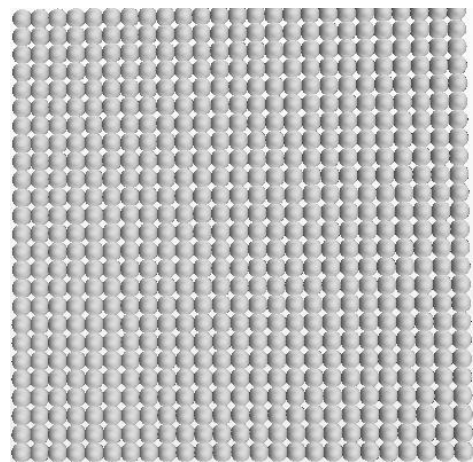
Figure 18: 3D macroalgae geometry (top view). Consist of single layer of spheres 25x25 with 3mm in diameter.

3.3   Geometry, mesh generation and boundary conditions.

Two sets of geometry will be used for 2D and 3D domain. One set with and the other one without the inner cylindrical assembly.

3.3.1 2D domain

For 2D modelling of cylindrical tank would be proper to use axisymmetric model, but unfortunately this model is not compatible with use of DEM model in Star-CCM+. Therefore the standard 2D model is used. The geometry was modelled according the dimensions from the validation experiment (Chapter 2.1.1) and it is shown in Figure 19. There is a good practice in modeling DEM particles that the particle shouldn't span over three or more cells in mesh. It may cause some solution errors. To avoid them, the coarser mesh will be used. When considering that the particle diameter is 3mm, then minimum cell size should be 3mm and higher. While modeling the mesh, following parameters in Table 2 were used. The final mesh is shown in Figure 20.

Base size	6 mm
Surface growth rate	1.1
Number of prism layers	3
Prism layer near wall thickness	3mm
Total thickness	12 mm

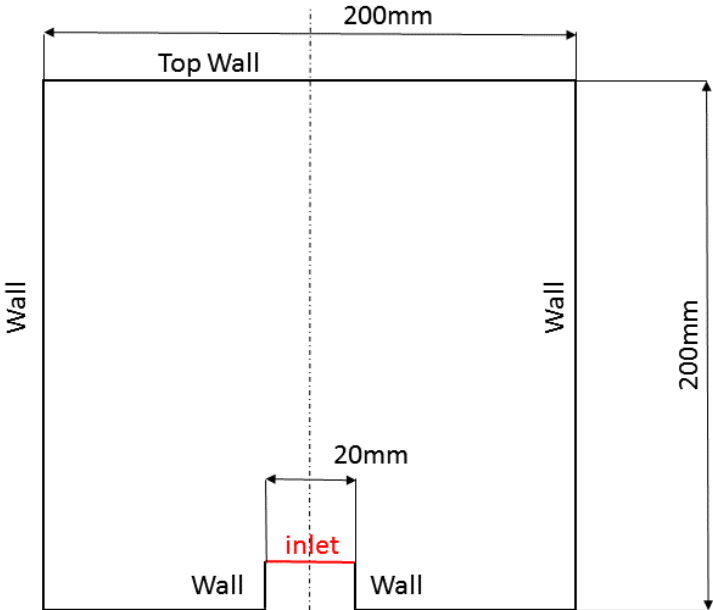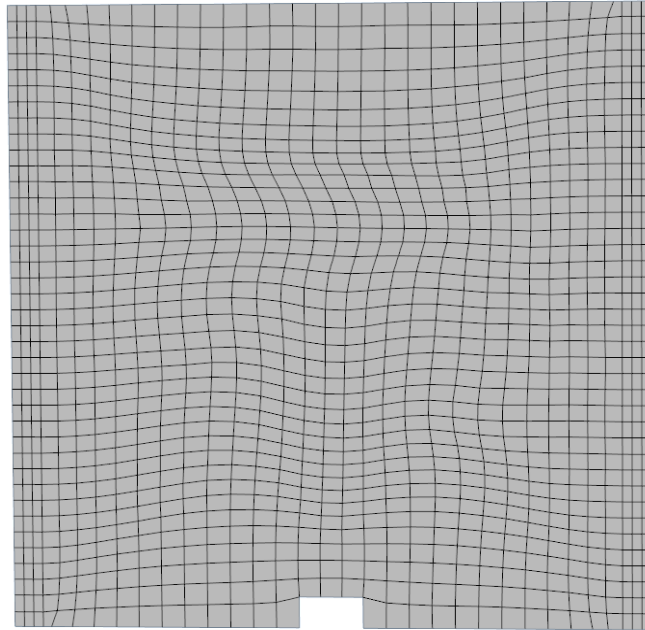*Table 2: Values used for the mesh generation.*

Figure 19: 2D geometry with its dimensions and boundaries.

Figure 20: Mesh used for 2D simulations.

3.3.2 2D domain with inner cylindrical assembly

The usage of the inner cylindrical assembly promises better flow pattern for growing macroalgae. The 2D representation of the inner cylinder is viewed as two baffles in a squared vessel. The dimensions were chosen accordingly, to have the same surface area in all sections (Figure 21). Thickness of the baffles corresponds to width on one mesh cell. The whole domain was meshed with same settings as described in chapter 3.3.1.
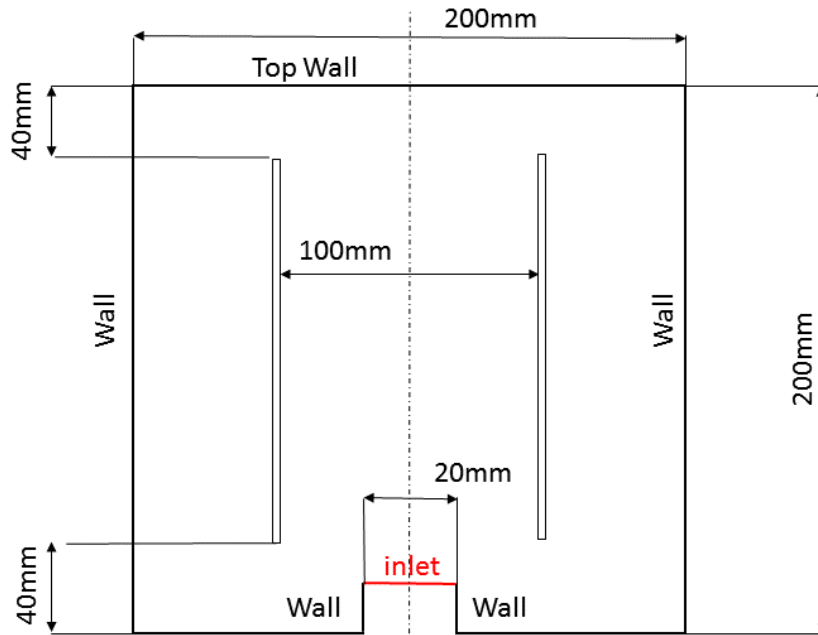
Figure 21: 2D geometry with inner cylindrical assembly.

3.3.3 3D domain

The geometry of 3D domain was modelled according dimensions in Figure 19. The base size for the mesh was set to 8mm, to speed up the simulation. Other settings were kept same as in Table 2. The final 3D mesh is shown in Figure 23.

3.3.4 3D domain with inner cylindrical assembly

In this case the domain is actually cylindrical so the flow area is divided into inner circle and outer circle. The diameter of the inner circle was chosen as a result of condition that the areas S_1 and S_2 are the same as it is shown on Figure 22. Then the diameter of the inner cylindrical assembly D_{in} is obtained from equation (3.1). The dimensions of the domain are shown in Figure 24. The whole domain was meshed with same settings as described in chapter 3.3.3.

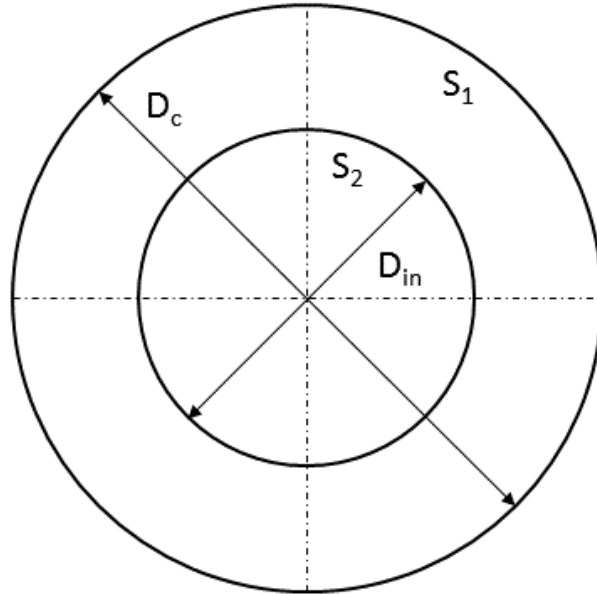$$\frac{\pi D_{in}^2}{4} = \frac{\pi(D_c^2 - D_{in}^2)}{4} \tag{3.1}$$

Figure 22: Sketched top view of cylindrical tank with inner cylindrical assembly. The diameter of the inner cylinder was chosen to match the condition $S_1 = S_2$.
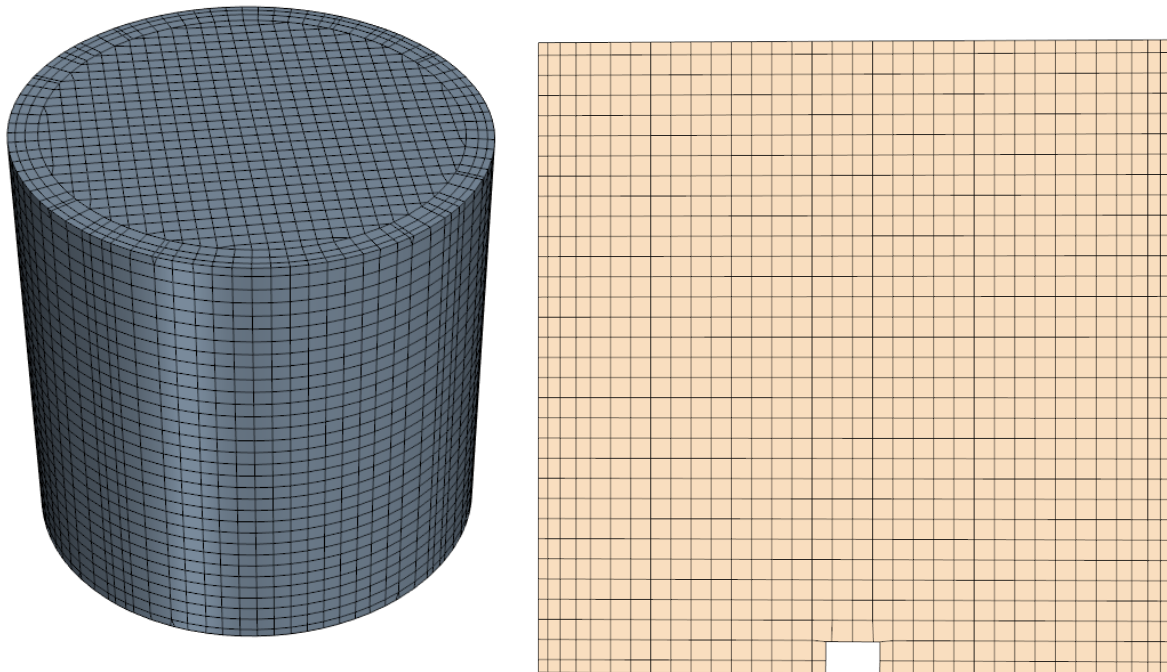

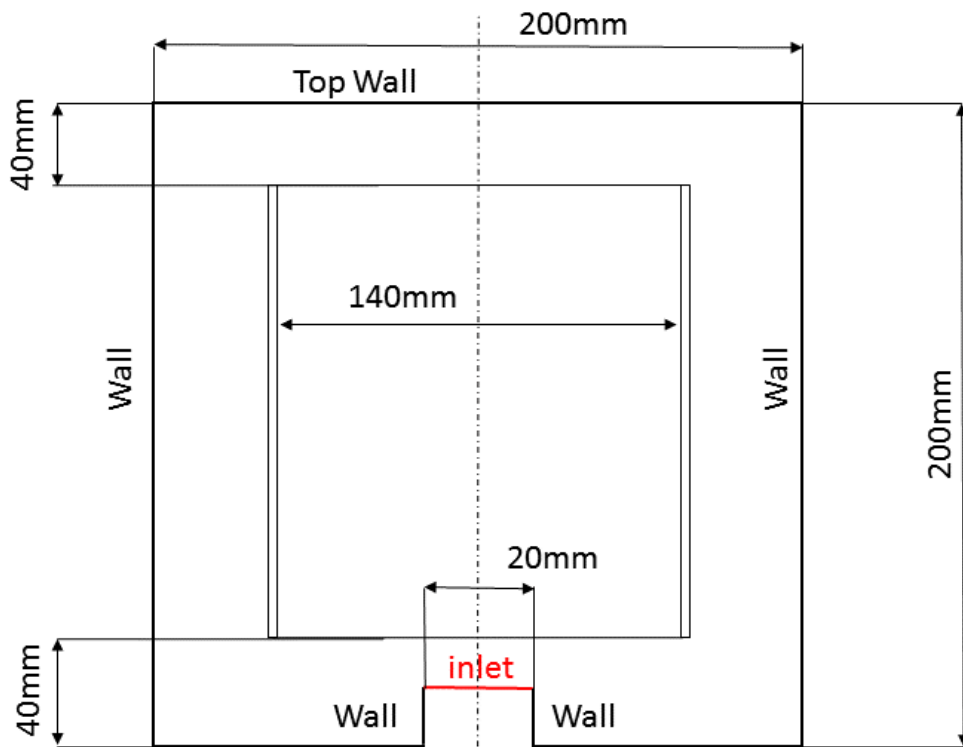*Figure 23: 3D mesh and cross section of 3D mesh.*

Figure 24: 3D geometry with inner cylindrical assembly.

3.4 Boundary conditions

To analyze the flow field in the domain in different states, the volume flow rate of air was chosen as a variable. As it is mentioned in chapter 2.1.1 the air volume flow rate was approximately $\dot{V} = 50$ l/h. In regards to validation experiment, the air volume flow rate will cover following values: [10; 25; 50; 75; 100] l/h. In order to maintain the same ratio of the air volume flow rate for both 2D and 3D domain, the value for 2D domain needs to be recalculated. The reason is that the volume flow rate applied in 2D needs the third dimension for the surface area, to calculate correct velocity. In Star-CCM+ 2D model assumes the third dimension (depth) to be **1 m**. The air volume flow rate for the 2D domain is recalculated according:

$$\dot{V}_{2D} = \frac{4 \cdot \dot{V}_{3D}}{\pi \cdot D_C}$$

(3.2)

41

D_c is cylindrical tank diameter. The recalculated values for all considered air volume flow rates are listed in Table 3. The air volume flow rate is applied in steady state model as Injector on the inlet boundary (shown in Figure 19) with size of an air bubble of 2 mm.

$\dot{V}_{3D}$ [l/h]	$\dot{V}_{3D}$ [m³/s]	$\dot{V}_{2D}$ [m³/s]
10	2.78E-06	1.77E-05
25	6.94E-06	4.42E-05
50	1.39E-05	8.84E-05
75	2.08E-05	1.33E-04
100	2.78E-05	1.77E-04

Table 3: Recalculated values for air volume flow rate.

On the top wall of the domain (Figure 19), which represents the free water surface, is set a slip wall condition. The rest of the walls are set with no-slip wall condition.

For inserting the particles into the domain in the transient model, a random injector is used. In 2D domain 30 particle clumps (Figure 17) are injected, to see the interaction between the particles. In 3D domain only one particle clump is injected into the domain, to reduce the computational time.

3.5 Physical model options and solver settings

Two physics model were used. Steady state physics model was used to initialize the flow field. Then the transient physics model was used for the DEM particles tracking.

3.5.1 Steady state physics model

2D/3D Segregated flow Gradients Gravity Constant density			
Liquid	water	Density = 1000 kg/m^3	
		Dynamic viscosity = 9e-4 Pa.s	
Turbulent			
RANS	K-Epsilon	Realizable K-Epsilon Two-Layer Exact Wall Distance Two-Layer All y+ Wall treatment	
Lagrangian multiphase	Air	Gas Constant Density Drag Force Material particles Pressure Gradient Force Shear Lift Force Spherical particles Two-way coupling	Density = 1.18 kg/m^3

3.5.2 Transient physics model

2D/3D Implicit Unsteady Segregated flow Gradients Gravity Constant density			
Liquid	water	Density = 1000 kg/m^3	
		Dynamic viscosity = 9e-4 Pa.s	
Turbulent			
RANS	K-Epsilon	Realizable K-Epsilon Two-Layer Exact Wall Distance Two-Layer All y+ Wall treatment	
Discrete Element Method			
Lagrangian multiphase	Seaweed	DEM Particles Particles Clumps Constant density Drag Force Pressure Gradient Force Track File	Density = 1.18 kg/m^3
		Solid	Density = 1000 kg/m^3 Poisson's Ratio = 0.1 Young's modulus = 10 kPa
Multiphase Interaction	Bond particles Hertz Mindlin	Bond radius multiplier = 0.1	

Values, which are not listed were left with default settings.

3.5.3 Solver settings

If parallel computation is used, it is good to enable Load Balancing for both physics models. It is located in Lagrangian multiphase solver and it will reduce the computational time. While using the transient physics, the time step was set to **0.01 s** and Segregated Flow solver was set to be frozen. Other settings were left by default. Physical time was chosen according the flow field to be able to capture several turns of the particles. It was within range 15 – 80 s.

4 Results and post processing

In this chapter the velocity fields in each domain will be compared and described. Then the particle tracks will be presented and further processed.

4.1 2D domain – Velocity fields

The velocity fields in the domain were compared for various air volume flow rates in the same scale to see the differences (

Figure 25). As an example velocity vectors for $\dot{V}$ = 100 l/h are shown in Figure 26, where the development of concentric vortices is clearly visible. The flow character matches to the expected results for cylindrical tank shown in Figure 14.
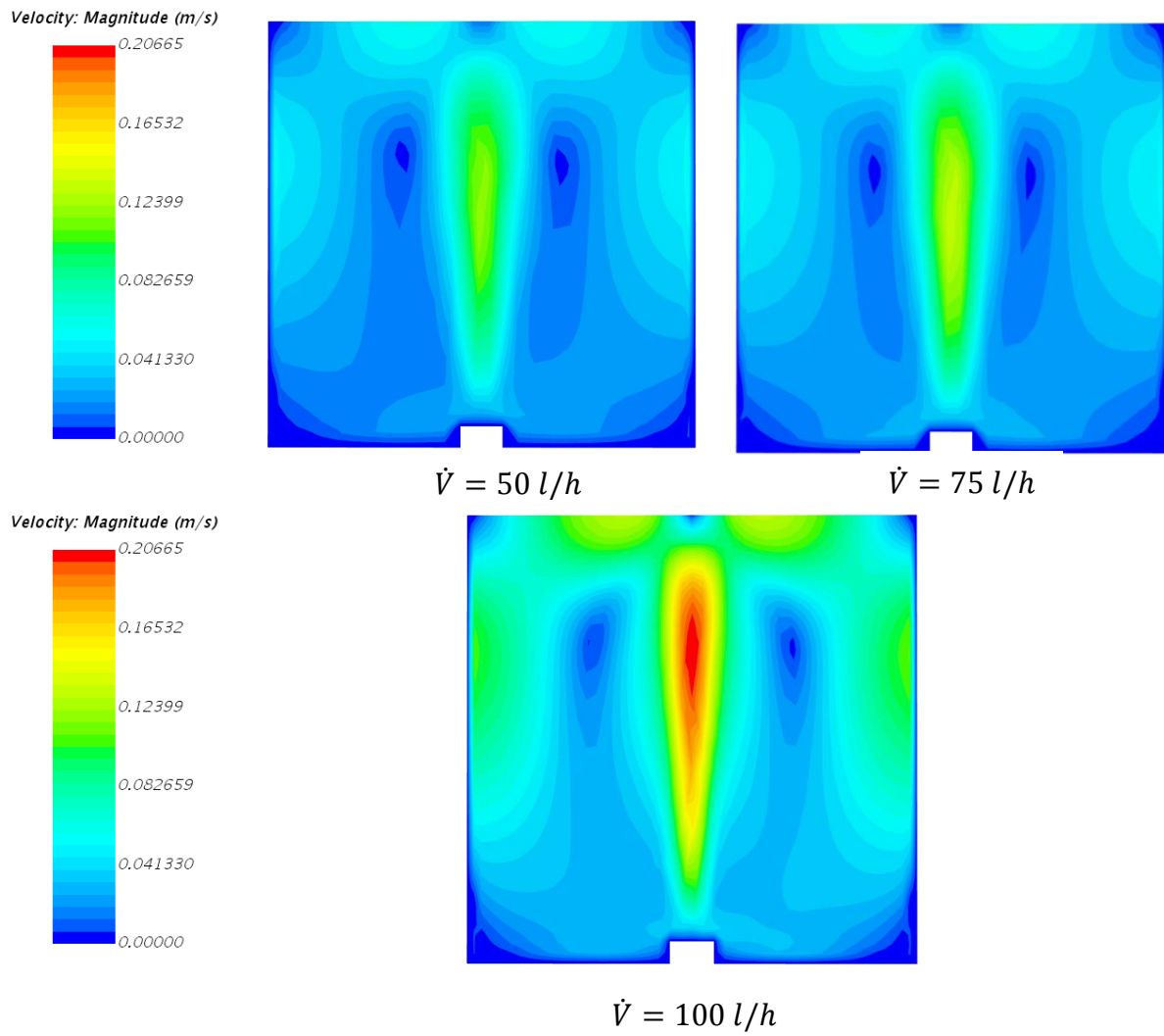

$$\dot{V} = 10 \; l/h \qquad\qquad \dot{V} = 25 \; l/h$$
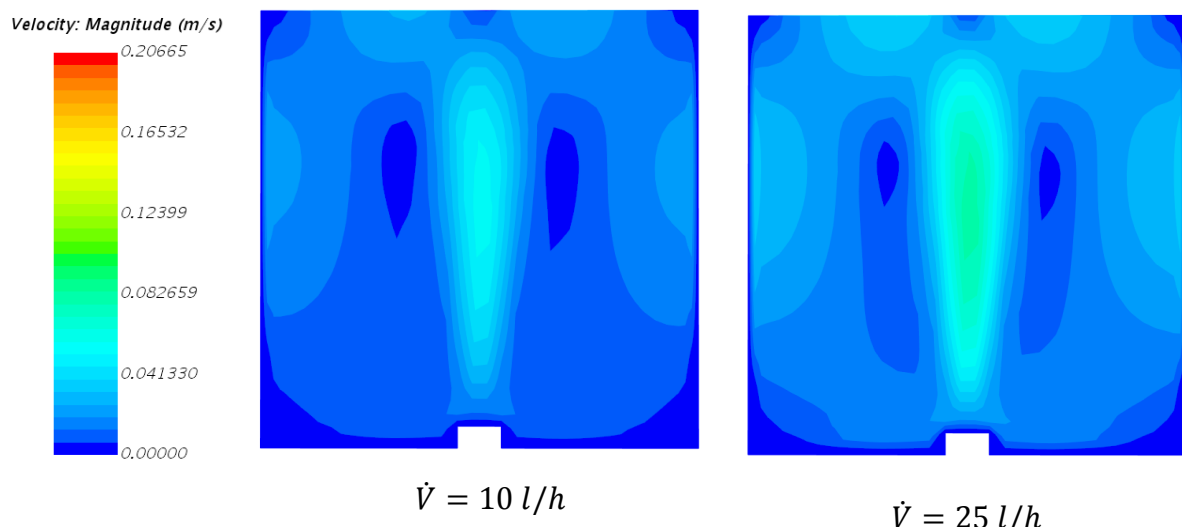
Figure 25: 2D domain - velocity fields in comparison for the same velocity scale.

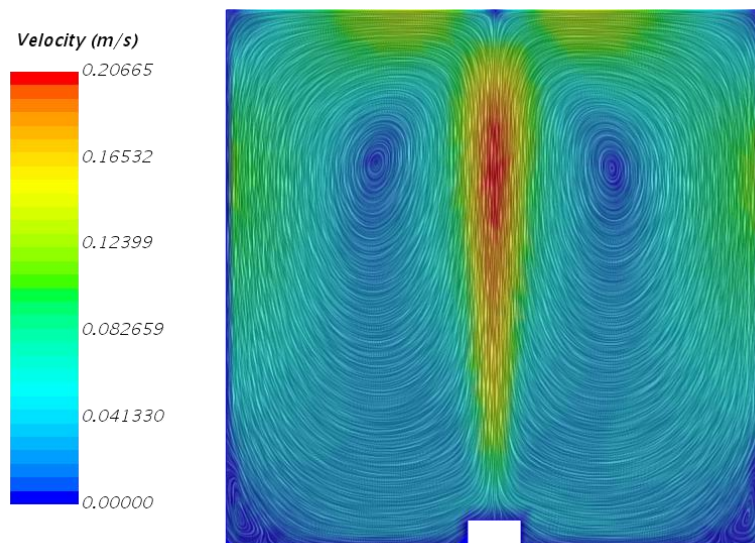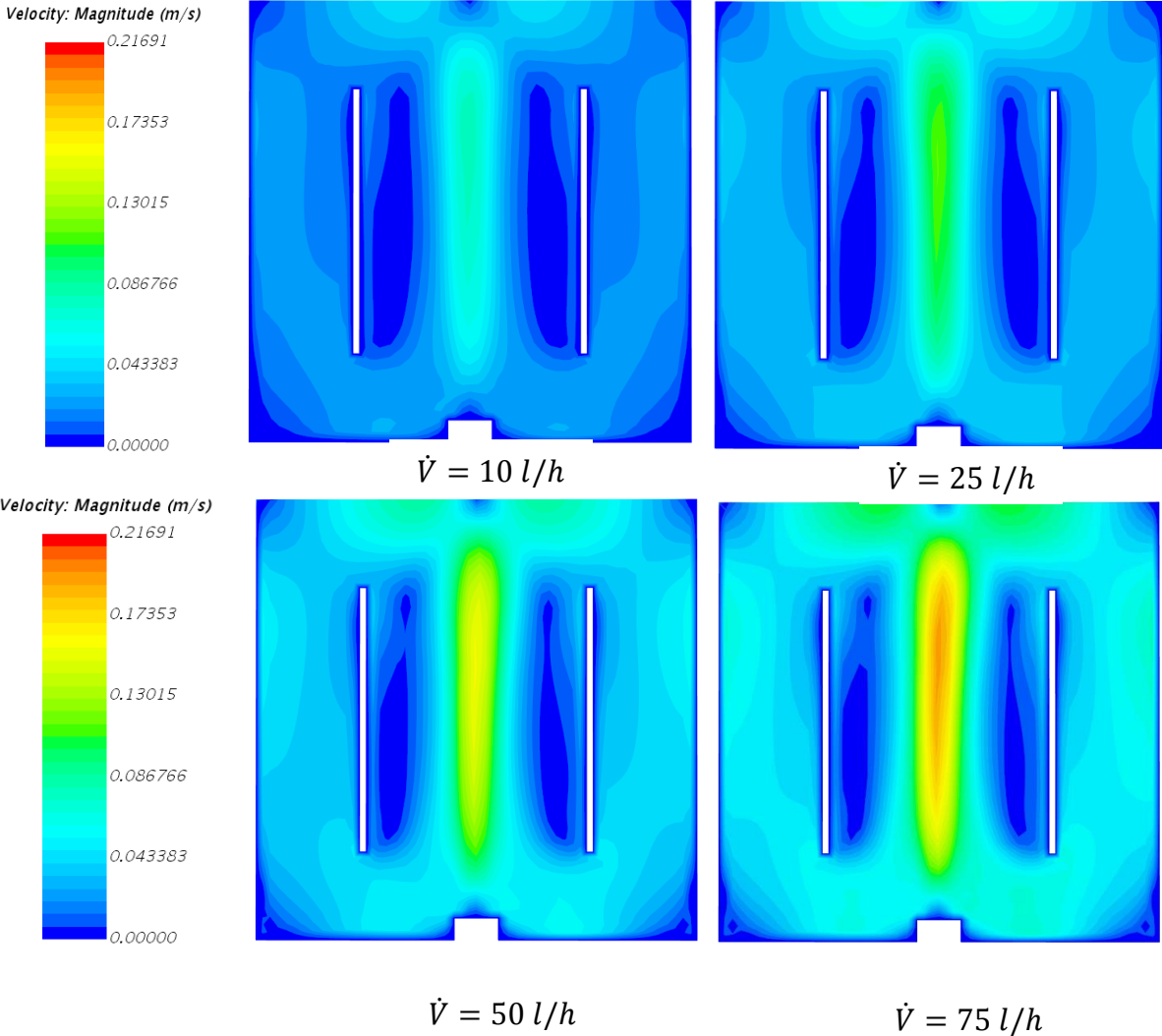*Figure 26: 2D domain – velocity vectors for volume air flow rate V̇=100 l/h.* Two concentric vortexes can be observed.

4.2 2D domain with inner cylindrical assembly – Velocity fields

The inner cylindrical assembly (draft tube) helps to distribute velocity field better in the bottom part of the tank, even for smaller air volume flow rates and provides better conditions for recirculation flow, then the domain without the inner cylinder. The velocity field comparison for different air volume flow rates is shown in Figure 27. As an example velocity vectors for $\dot{V}$= 100 l/h are shown in Figure 28, where the flow distribution around the inner cylinder is clearly visible.

$\dot{V} = 10 \; l/h$

$\dot{V} = 25 \; l/h$

$\dot{V} = 50 \; l/h$

$\dot{V} = 75 \; l/h$
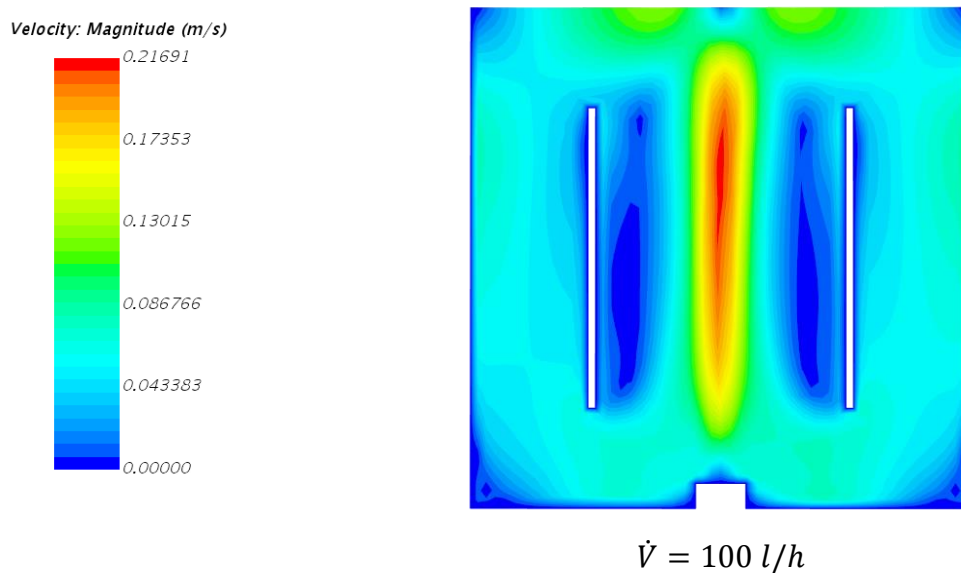
$$\dot{V} = 100 \; l/h$$

Figure 27: 2D domain with inner cylindrical assembly – velocity fields in comparison for the same velocity scale.

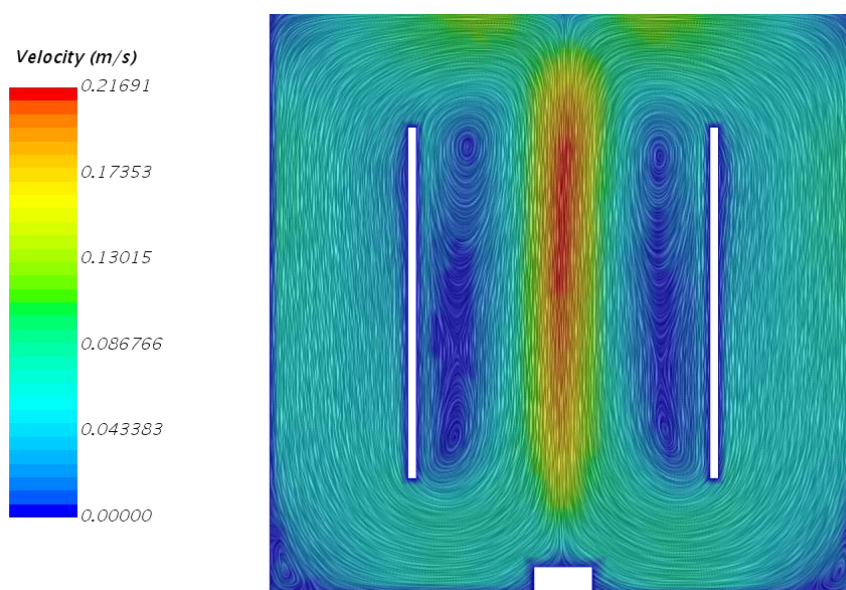*Figure 28: 2D domain with cylindrical assembly – velocity vectors for volume air flow rate V =100 l/h. Two concentric vortexes can be still seen, but majority of the fluid flows around the inner cylinder and increases velocity in the bottom part of the tank.*

4.3 3D domain – Velocity fields

The velocity fields, shown in the cross-sections, for two different air volume flow rates are presented for the same velocity scale in

Figure 29. As an example velocity vectors for $\dot{V}$ = 100 l/h are shown in cross-section and presented in Figure 30. The results from the 3D simulations show quite different flow patterns in comparison to the 2D simulation results. The bottom part of the tank doesn't how such a big velocity gradient even for higher air flow rates, which wasn't expected and it may cause some inaccurate results in particle tracking.

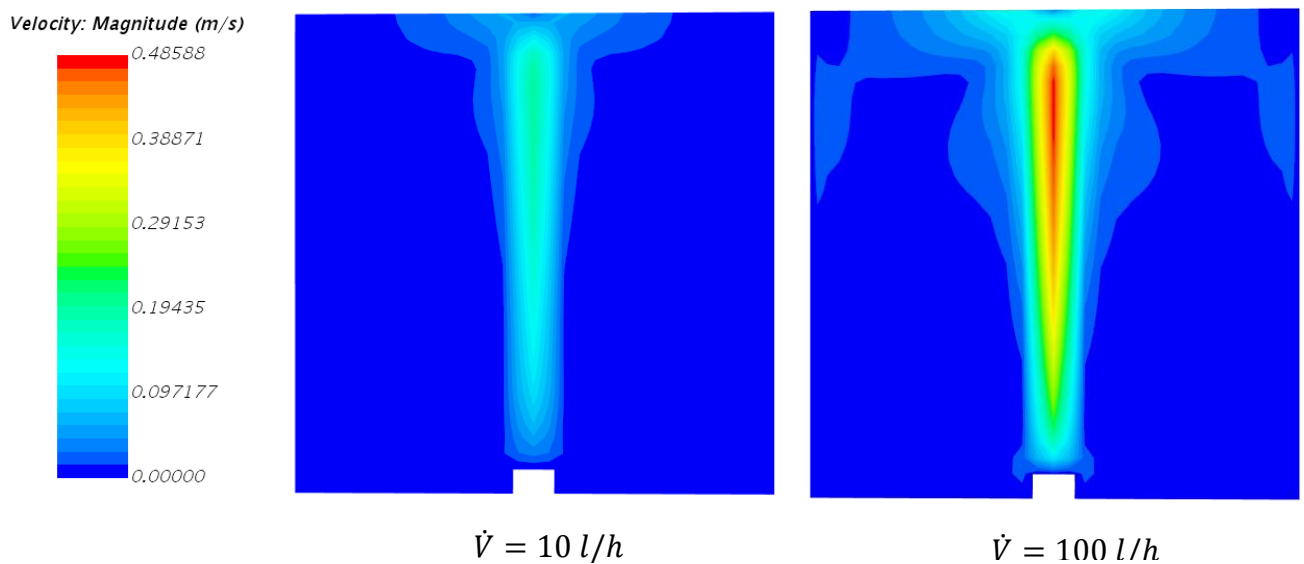$$\dot{V} = 10 \; l/h \qquad\qquad \dot{V} = 100 \; l/h$$

Figure 29: 3D domain – cross section view. Velocity fields shown in comparison for the same velocity scale. The velocity gradient is visible mainly near around the main jet stream and does not develop in the rest of the domain, particularly in the bottom part.
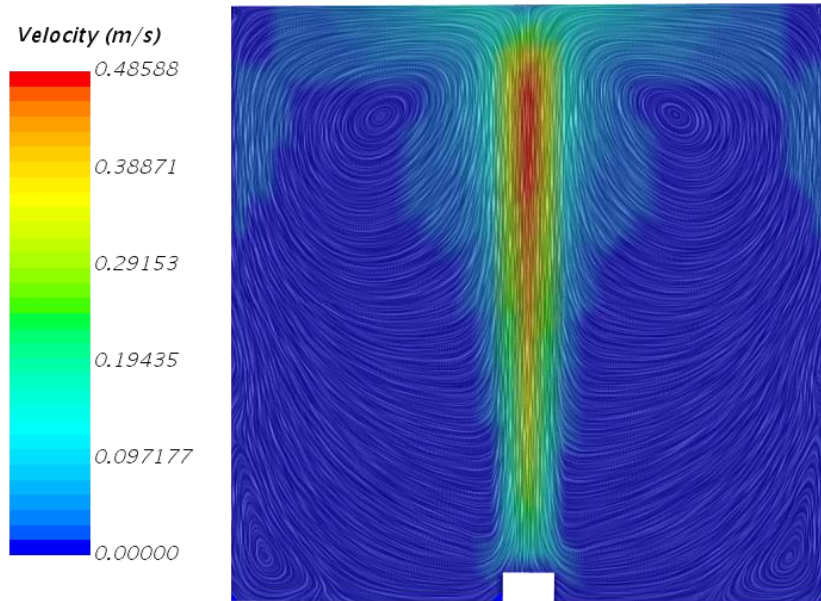
Figure 30: 3D domain – cross-section view. Velocity vectors for volume air flow rate V =100 l/h. Two concentric vortexes can be still observed in the top part of the domain.

4.4   3D domain with inner cylindrical assembly – Velocity fields

The velocity fields, shown in the cross-sections, for two different air volume flow rates are presented in

Figure 31. As an example velocity vectors for $\dot{V}$= 100 l/h are shown in cross-section and presented in Figure 32. The results show that the inner cylindrical assembly significantly helps to distribute the velocity field to the bottom part of the domain and provides better condition for recirculation, then the domain without inner cylinder.
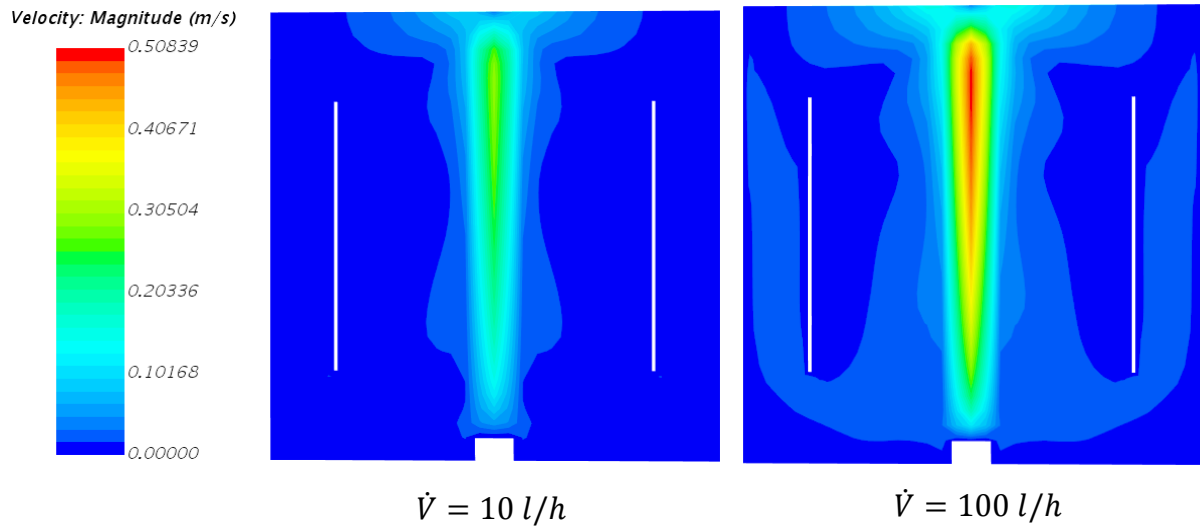
$$\dot{V} = 10 \ l/h \qquad \dot{V} = 100 \ l/h$$

Figure 31: 2D domain with inner cylindrical assembly – cross-section view. Velocity fields in comparison for the same velocity scale.
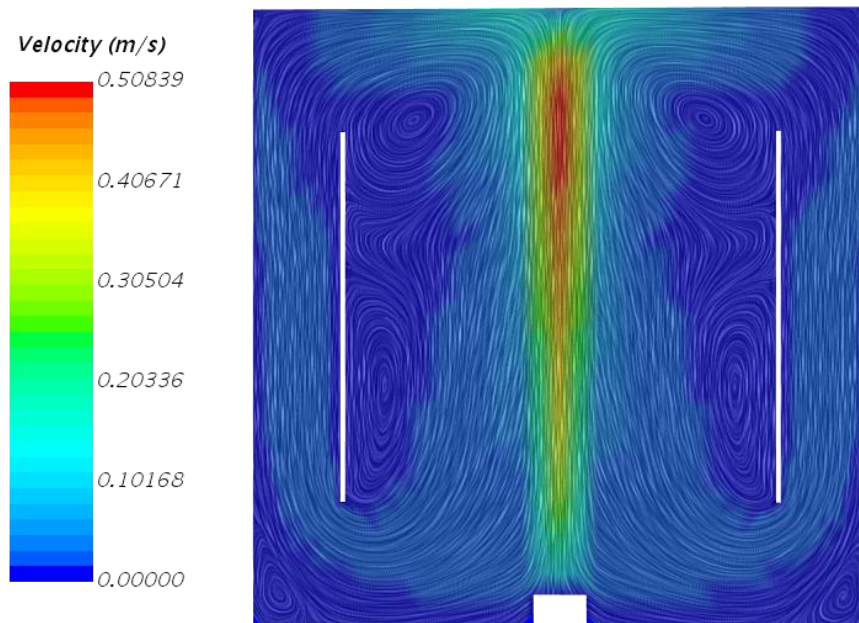

Figure 32: 3D domain with cylindrical assembly – cross-section view. Velocity vectors for volume air flow rate $\dot{V}$=100 l/h. Multiple concentric vortexes can be seen, but majority of the fluid flows around the inner cylinder and increases velocity in the bottom part of the tank.

4.5 2D domain – Particle tracking

In 2D case, 31 particle clumps were randomly injected into the developed velocity field. Particle tracking was applied on one particle clump and its path can be seen in Figure 33 for the domain without inner cylinder an in Figure 35 for domain with inner cylinder. The figures show that the usage of the inner cylindrical assembly provides better distribution of particles inside the domain and more regular periodicity. This claim is also supported by visualization of vertical position of particle in time shown in Figure 36, where more regular periodicity can be observed with usage of inner cylinder.
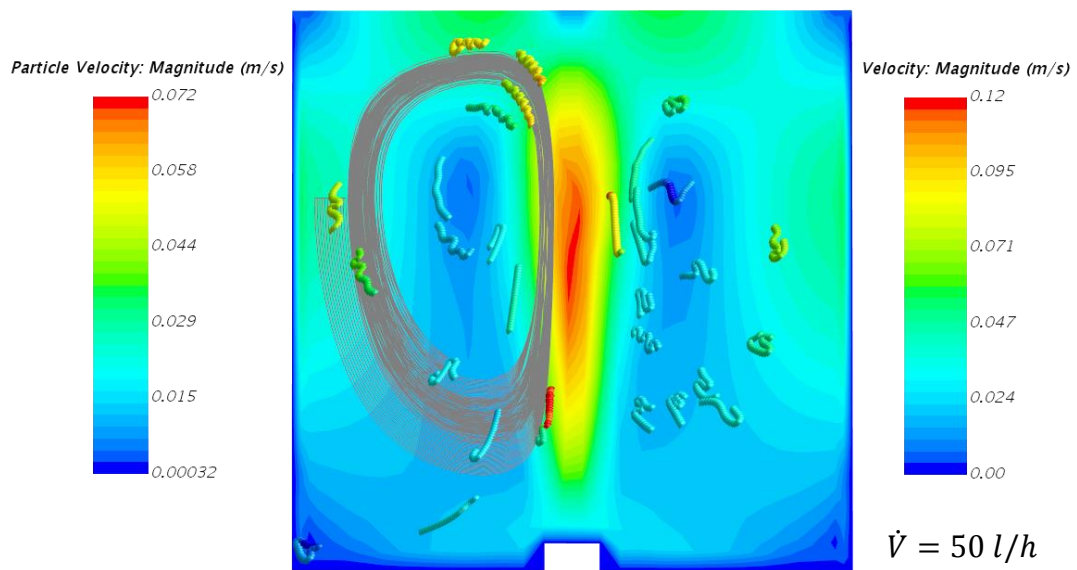

$$\dot{V} = 50 \; l/h$$

Figure 33: 2D domain with injected particle clumps. The particle track path of one particular particle clump is visualized with grey lines.
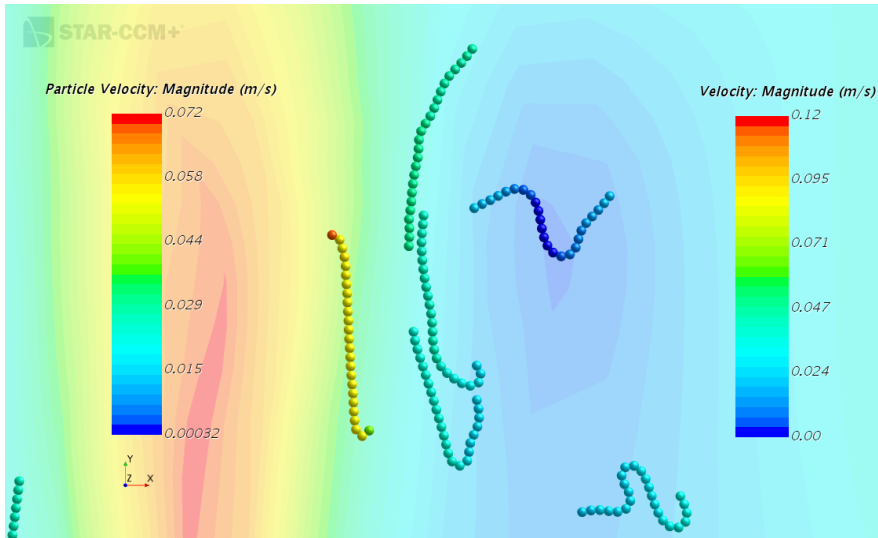
Figure 34: 2D domain - detailed view on particle clumps. The particles are flexible and they are able to interact with each other.
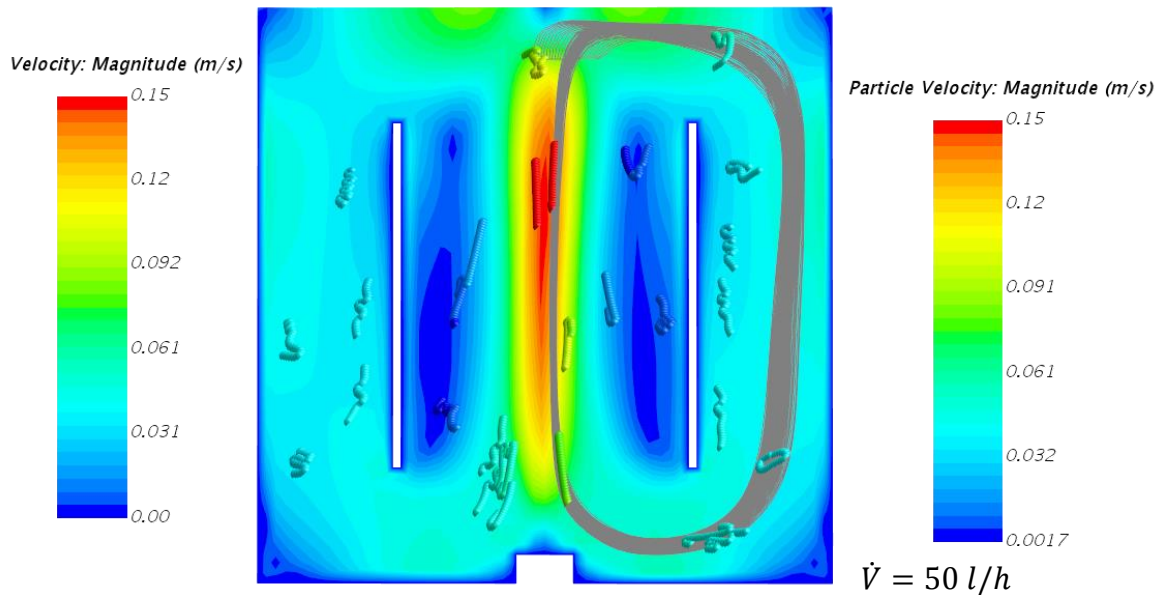

$$\dot{V} = 50 \, l/h$$

Figure 35: 2D domain with inner cylindrical assembly and injected particle clumps. The particle track path of one particular particle clump is visualized with grey lines. The use of inner cylinder provides better distribution of the particle clumps over the domain.

4.6 2D Model's description

The track files were obtained for variation of air volume flow rates and post-processed with Matlab/Octave code presented in Appendix I. The code plots particle's vertical position in time (example shown in Figure 36) and calculate average time for particle to complete one cycle. This cycle can be understood as a period of an intermittent light-dark cycle T_c mentioned in chapter 1.2. To mathematically describe aerated system used for the macroalgae cultivation, another variable needs to be introduced. This variable will be called specific aeration rate (SAR) and it is defined as:

$$\text{SAR} = \frac{\dot{V}}{V} \quad [s^{-1}]$$

(4.1)

$\dot{V}$ is air volume flow rate [m³/s] and V represents the volume of the aerated tank [m³]. Then the aerated system can be described as a $T_c = f(SAR)$. The collected data from the 2D model (Table 4) were plotted in Figure 37 and interpolated with power function. The result of the mathematical description for the 2D aerated system without inner cylindrical assembly is described by equation (4.2) and the 2D aerated system with inner cylindrical assembly is described by equation (4.3).
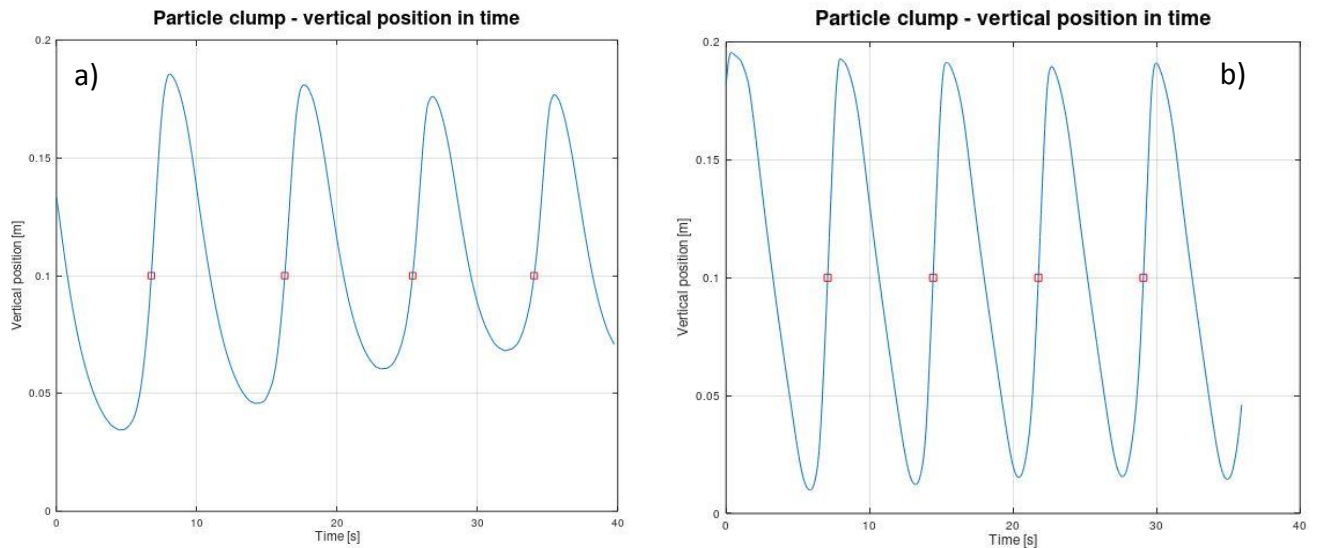

Figure 36: Vertical position of the particle clump in time for $\dot{V}$ = 50 l/h: a) 2D domain without inner cylinder. b) 2D domain with inner cylinder.

54

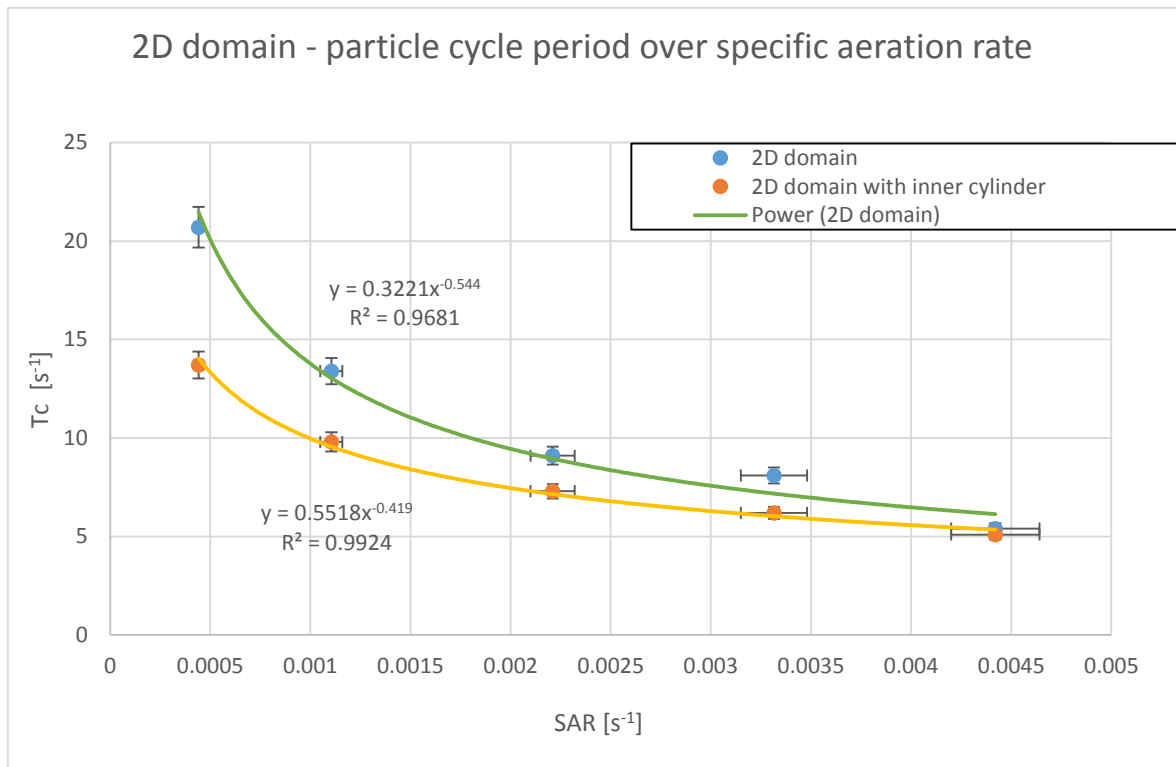| $\dot{V}$ [m³/s]	$\dot{V}_{2D}$ [m³/s]	$\dfrac{\dot{V}}{V}$ [s⁻¹]	$T_c -$ without cylinder [s⁻¹]	$T_c -$ with cylinder [s⁻¹]
10	1.76839E-05	0.000442	20.7	13.7
25	4.42097E-05	0.001105	13.4	9.8
50	8.84194E-05	0.00221	9.1	7.3
75	0.000132629	0.003316	8.1	6.2
100	0.000176839	0.004421	5.4	5.1

Table 4: Collected data from the 2D model.

Figure 37: 2D domain - particle cycle period over specific aeration rate.

2D system without inner cylinder –
$$T_c = 0.3221 \cdot \left(\frac{\dot{V}}{V}\right)^{-0.54} \tag{4.2}$$

2D system with inner cylinder –
$$T_c = 0.5518 \cdot \left(\frac{\dot{V}}{V}\right)^{-0.42} \tag{4.3}$$

55

4.7 3D domain – Particle tracking

In 3D case, only one particle clump was randomly injected into the velocity field. Particle paths can be seen in Figure 38 for the domain without inner cylinder an in Figure 40 for domain with inner cylinder. The figures show that the usage of the inner cylindrical assembly provides better distribution of particles inside the domain, which is also confirmed in 2D model.
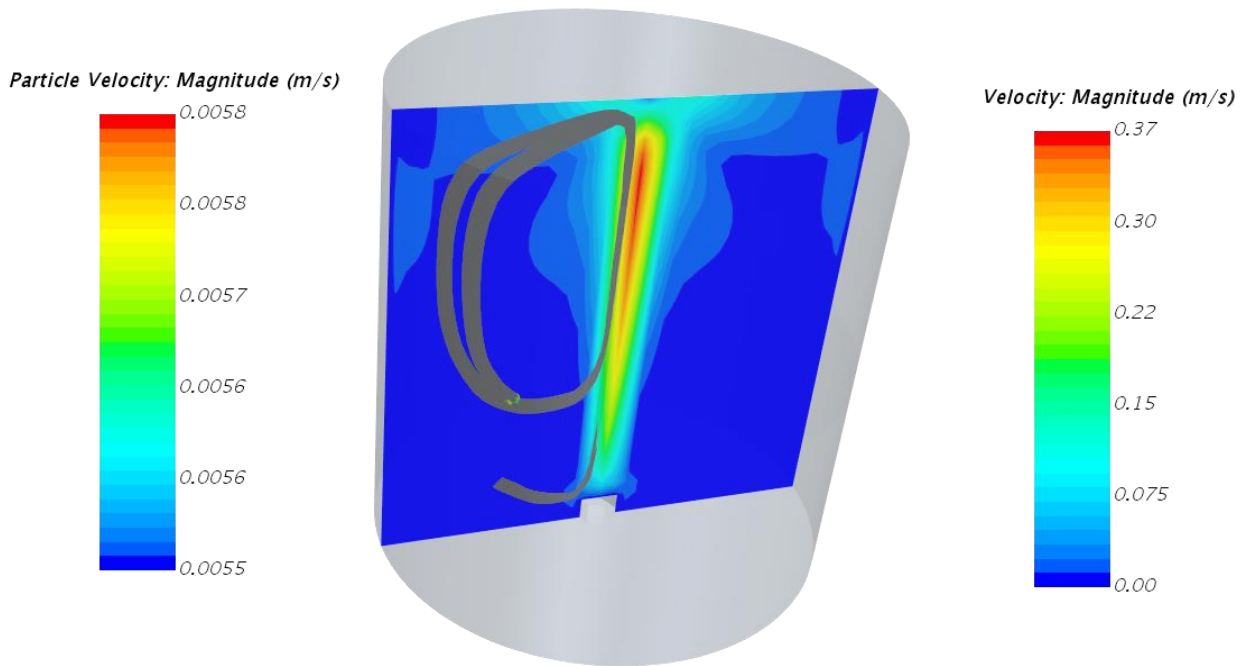
Figure 38: 3D domain with injected particle clump. The particle track path is visualized with grey lines. It can be seen, that the particle clump firstly spawned in the bottom part of the domain, remains circulating in upper 2/3 of the domain.

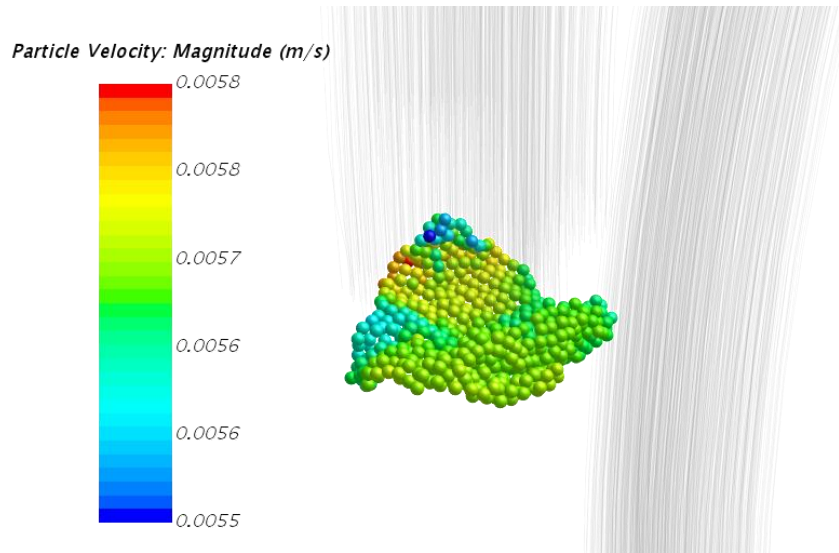*Figure 39: 3D domain – detailed view on a particle clump. The plasticity of the particle clump can be observed as it is shaped by surrounding flow of liquid.*
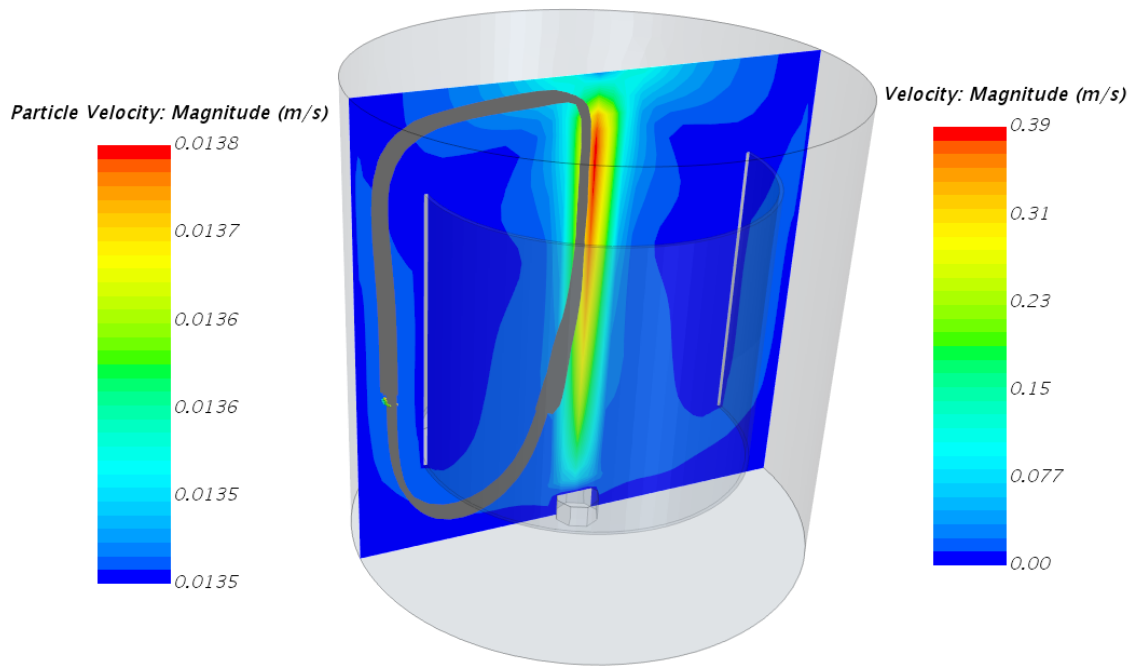

Figure 40: 3D domain with inner cylindrical assembly and injected particle clump. The particle track path is visualized with grey lines. The use of inner cylinder provides better distribution of the particle clumps over the domain, which is also confirmed in 2D model.

4.8 3D model's description

The track files were obtained for variation of air volume flow rates and post-processed with Matlab/Octave code presented in Appendix I, as well as in 2D model. As an example, plotted vertical position of the particle clump in time is shown in Figure 41. The 3D model shows that, the longer time is needed for the particle clump to complete the cycle. This is resulted by the character of the velocity field inside the domain. The collected data from the 3D model (Table 5) were plotted in Figure 42 and interpolated with power function. The result of the mathematical description for the 3D aerated system without inner cylindrical assembly is described by equation (4.4) and the 3D aerated system with inner cylindrical assembly is described by equation (4.5).
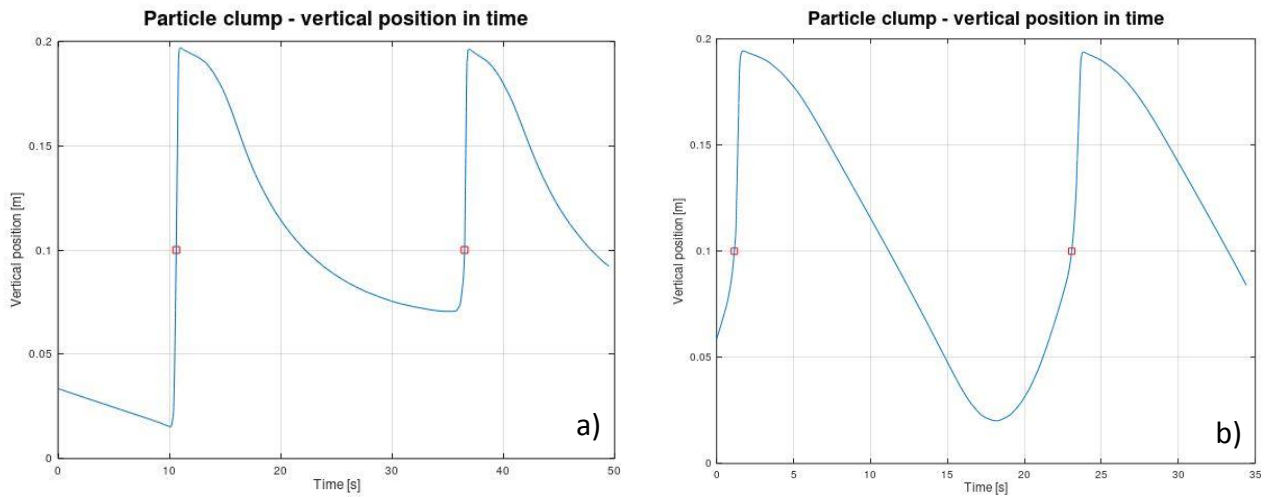
Figure 41: Vertical position of the particle clump in time for $\dot{V}$ = 50 l/h: a) 3D domain without inner cylinder. b) 3D domain with inner cylinder.

$\dot{V}$ [m³/s]	$\dot{V}_{3D}$ [m³/s]	$\dfrac{\dot{V}}{V}$ [s⁻¹]	T_c − without cylinder [s⁻¹]	T_c − with cylinder [s⁻¹]
10	1.76839E-05	0.000442	53.3	30.3
25	4.42097E-05	0.001105	33.4	30.2
50	8.84194E-05	0.00221	25.9	21.9
75	0.000132629	0.003316	22.9	19.1
100	0.000176839	0.004421	19.9	17.1

Table 5: Collected data from the 3D model.

Figure 42: 3D domain - particle cycle period over specific aeration rate.

3D system without inner cylinder –
$$T_c = 2.06 \cdot \left(\frac{\dot{V}}{V}\right)^{-0.42} \tag{4.4}$$

3D system with inner cylinder –
$$T_c = 4.27 \cdot \left(\frac{\dot{V}}{V}\right)^{-0.265} \tag{4.5}$$

5 Conclusion

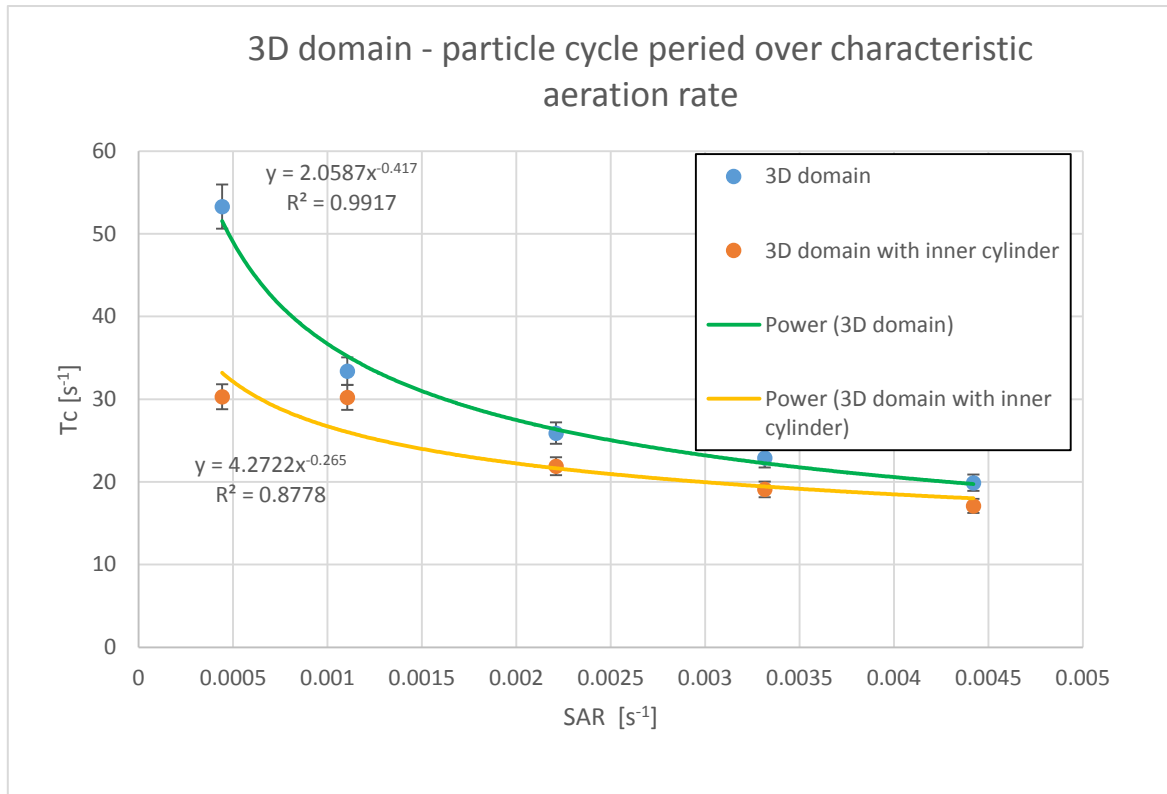The purpose of this paper was to describe and test a possible approach of modelling aerated systems for macroalgae cultivation purposes with a use of CFD code. It was found that the best approach for modelling of the macroalgae movement within those systems is to use Discrete Element Method with a Particle Clumps model. This model is included in Star-CCM+ code, which was used for the analysis. Two models of aerated systems were created, one 2D and one 3D. Both models were supposed to represent the aerated cylindrical tank, but in case of the 2D model it was not possible, due to the incompatibility of axisymmetric model with DEM. Then the 2D model can be used to describe a rectangular-shape tanks with good precision and low cost. Also the impact of using inner assembly (draft tube) inside the tank was analyzed. The results shows that the inner assembly provides better distribution of the velocity field inside the tank and it can reduce the recirculation time for the macroalgae, specifically for the smaller aeration rates (see Figure 37 and Figure 42). Furthermore, parameters of the mathematical correlation between the macroalgae's recirculation period and specific aeration rate were identified, which is presented by equations (4.2), (4.3), (4.4) and (4.5). These correlations can be used in Integrated Multi Trophic Aquaculture production systems to set the optimal conditions for the macroalgae cultivation.

Although the created models are just prove of the concept, they clearly show that it is possible to model the aerated systems with macroalgae motion. Still many assumptions and simplifications were made (chapter 3.2), that is why the level of the precision is questionable. Nevertheless this paper is one of the first researches conducted in combining CFD and Integrated Multi Trophic Aquaculture production systems, so there is still enough space for improvement. Also more experiments need to be performed to validate the CFD results. Few points for further improvements are listed:

- Using finer mesh to capture the flow field more precisely.
- Performing mesh size dependency analysis.
- Application of transient flow field with DEM particle tracking

6 Bibliography

[1]   RICHMOND, Amos. Biological Principles of Mass Cultivation. *Handbook of Microalgal Culture: Biotechnology and Applied Phycology*. 2004, s. 125-177. ISBN 0–632–05953–2.

[2]   B. Rehak, S. Celikovsky and S. Papacek, "Model for Photosynthesis and Photoinhibition: Parameter Identification Based on the Harmonic Irradiation O2 Response Measurement," in *IEEE Transactions on Automatic Control*, vol. 53, no. Special Issue, pp. 101-108, Jan.2008. URL: http://ieeexplore.ieee.org/stamp/stamp.jsp?tp=&arnumber=4439824&isnumber=4439798

[3]   P.H.C. Eilers, J.C.H. Peeters, A model for the relationship between light intensity and the rate of photosynthesis in phytoplankton, Ecological Modelling, Volume 42, Issues 3–4, 1988, Pages 199-215, ISSN 0304-3800, https://doi.org/10.1016/0304-3800(88)90057-9.

[4]   MATONOHA Ctirad, Štěpán PAPÁČEK a Dalibor ŠTYS. *Model of Photosynthesis and Photoinhibition in Microalgae: A Singularly Perturbed Problem*. 2010, ,0-11. URL: http://www.cs.cas.cz/matonoha/download/V1114.pdf

[5]   Dolinek P.: Couette - Taylorův fotobioreaktor, Diplomova prace ČVUT, 2007.

[6]   GLENN, Kyle William. Tissue mechanical traits dictate hydrodynamic performance. *Evolutionary Ecology of Seaweed Strength and Flexibility*. s. 10-36.

[7]   James M. Ebeling, Michael B. Timmons, J.J. Bisogni, Engineering analysis of the stoichiometry of photoautotrophic, autotrophic, and heterotrophic removal of ammonia–nitrogen in aquaculture systems, Aquaculture, Volume 257, Issues 1–4, 2006, Pages 346-358. URL: http://www.sciencedirect.com/science/article/pii/S004484860600216X

[8]   Ilan Halachmi, Yitzchak Simon, Rami Guetta, Eric M. Hallerman, A novel computer simulation model for design and management of re-circulating aquaculture systems, Aquacultural Engineering, Volume 32, Issues 3–4, 2005, Pages 443-464, ISSN 0144-8609. URL: http://www.sciencedirect.com/science/article/pii/S0144860904000974

[9]   BREGNBALLE, Jacob. *A Guide to Recirculation Aquaculture*. 2015.

[10]   Schugerl, K., Bellgardt, K. H.: Bioreaction Engineering, Modeling and Control, Springer

- Verlag, Berlin Heidelberg (2000).

[11]   Tamiya, H. (1957) Mass culture of algae. Ann. Rev. Plant Physiol., 8, 309.

[12]   BHASKARAN,   Rajesh   a   Lance   COLLINS. *Introduction   to   CFD   Basics*. URL: http://dragonfly.tam.cornell.edu/teaching/mae5230-cfd-intro-notes.pdf

[13]   H K Versteeg a W Malalasekera. *An Introduction to Computational Fluid Dynamics: THE FINITE VOLUME METHOD*. 2007. ISBN 978-0-13-127498-3.

[14]   F. Moukalled, L. Mangani a M. Darwish. *The Finite Volume Method in Computational Fluid Dynamics: An Advanced Introduction with OpenFOAM® and Matlab®*. ISBN 978-3-319-16873-9.

[15]   Eggenspieler, G., Turbulence Modeling (ANSYS manuals), ANSYS, Inc., 2011

[D16]   DAVIS, Mark. *Finite Difference Methods*. Department of Mathematics Imperial College London, 2011.

[17]   VLČEK, Petr. *MODELOVÁNÍ TURBULENTNÍHO PROUDĚNÍ*. , 21.

[18]   C. WILCOX, David. *Turbulence Modeling for CFD*. Third Edition. 2006.

[19]   KOZUBKOVÁ, Milada a Sylva DRÁBKOVÁ. *Numerické modelování proudění FLUENT I*. Ostrava: Vysoká škola báňská - Technická univerzita Ostrava, 2003, 115 s. ISBN 80-248-0525-1.

[20]   Tey Wah-Yen, Yutaka Asako, Nor Azwadi Che Sidik a Goh Rui-Zher. *Governing Equations in Computational Fluid Dynamics: Derivations and A Recent Review*. 2017, , 20.

[21]   BLEJCHAŘ, Tomáš. *TURBULENCE MODELOVÁNÍ PROUDĚNÍ - CFX*. 2012. ISBN 978-80-248-2606-6.

[22]   Ren, K & Hu, Junling & Xiong, Xingguo & Zhang, Linfeng & Wei, J. (2009). Validation of Turbulence Models in STAR-CCM+ by N.A.C.A. 23012 Airfoil Characteristics.

[23]   Simcenter   Star-CCM+   Product   documentation,   2018. URL: https://documentation.thesteveportal.plm.automation.siemens.com/

[24]   SUBRAMANIAM, Shankar. *LagrangianeEulerian methods for multiphase flows*. Department of Mechanical Engineering, Iowa State University, 2080 H.M. Black Engineering, Ames, IA 50011, United States, 2012, , 31.

[25]   Oca, J., Machado, S., Jimenez de Ridder, P., Cremades, J., Pintado, J., Masal_o, I. (2016) Comparison of two water agitation methods in seaweed culture tanks: inuence of the rotating velocity in the seaweed growth and energy requirement. EAS2016 - Food for thought, pp. 716-717. Edinburgh, Oct 2016.

[26]   Papacek, S., Matonoha, C., Petera, K. (2018) Modeling and Simulation of Microalgae Growth in a Couette-Taylor Bioreactor. In: Kozubek, T., ermk, M., Tich, P., Blaheta, R., stek, J., Luk, D, Jaro, J. (Eds), Lecture Notes in Computer Science 11087. 3rd Inter-

national Conference on High Performance Computing in Science and Engineering, HPCSE

2017, Karolinka, Czech Republic, 174187.

[27]   Johnson, K.L. 1987. Contact Mechanics, Cambridge University Press, Cambridge.

[28]   Rayleigh, L. 1885. "On waves propagated along the plane surface of an elastic solid", Proc. Lond. Math. Soc. 17.

[29]   Timoshenko, S. 1951. Theory of Elasticity, McGraw-Hill Book Company.

[30]   FUTRZYNSKI, Romain. Speeding up Particle Clumps DEM simulations [online]. In: . 29.6.2018,   s.   4   [cit.   2018-12-30]. URL: https://thesteveportal.plm.automation.siemens.com/articles/en_US/FAQ/Speeding-up-Particle-Clumps-DEM-simulations?type=pdf

[31]   Project: Computational and experimental assessment of the flow pattern within a macroalgae production system. URL: http://auc.cz/scholaludus/projects/papacek.php

7 Appendix I

Code for Matlab/Octave to post-process track file data.

```
1
2 d = dlmread('3d_v50.csv', ',', 1, 0);
3 size(d)
5 y = d(:,4);
6 t = d(:,1);
7 num = length(t)
9 ym = 0.1; % height where the particles are monitored
10
11 figure(1);
12 tm = [ ];
13 np = 0;
14
15 if ( y(1) < ym )
16 vz = 0
17 else
18 vz = 1
19 end
20
21 for i=2:num
22
23 if ( t(i) < t(i-1) )
24 plot(t(1:i-1), y(1:i-1));
25 break;
26 end
27
28 if ( vz == 0 )
29 if ( y(i) > ym )
30 np = np+1;
31 tm(np) = t(i);
32 ks = (y(i)-y(i-1))/(t(i)-t(i-1)); tm(np) = t(i-1)+(ym-y(i-1))/ks;
33 plot(tm(np),ym,'rs');
34 if ( np == 1 );
35 hold on; end
36 vz = 1;
37 end
38 else
39 if ( y(i) < ym )
40 vz = 0;
41 end
42 end
43 end
44 hold off;
45 grid on;
46 title('Particle clump - vertical position in time','fontsize',18);
47 xlabel('Time [s]','fontsize',12);
48 ylabel('Vertical position [m]','fontsize',12);
50 tm
51 np
53 sum = 0;
54 for i=2:np
55 sum = sum+(tm(i)-tm(i-1));
56 end
57 sum
58 tp = sum/(np-1)
59 fprintf('\n number of periods: %d \n average time period: %g\n\n',np,tp
```

The beginning of the data obtained from particle tracking shown for an illustration:

Track: Time (s)	Track: Position[X] (m)	Track: Position[Y] (m)	Track: Position[Z] (m)
9.16E-05	-0.050168408	-0.016756173	0.033556687
0.253507976	-0.049863355	-0.019328668	0.033102863
1.352887511	-0.047650824	-0.018765403	0.031124508
2.456647992	-0.045358247	-0.018179114	0.029141855
4.060512185	-0.041599972	-0.017006253	0.026292016
5.601679564	-0.037868082	-0.015800553	0.023550137
6.647220373	-0.034668074	-0.014616	0.021697258
7.76080513	-0.031002003	-0.01320798	0.019730859
8.509912968	-0.027801993	-0.011878359	0.018386582
9.162179947	-0.024522694	-0.01054017	0.01715297
9.554308891	-0.02132267	-0.009306113	0.016318509